Materials and Design 200 (2021) 109457

Contents lists available at ScienceDirect

Materials and Design

journal homepage: www.elsevier.com/locate/matdes

Cost-affordable and qualified powder metallurgy metastable beta titanium alloy by designing short-process consolidation and processing

Qinyang Zhao [a,b,*], Yongnan Chen [a], Yiku Xu [a], Rob Torrens [b], Leandro Bolzoni [b], Fei Yang [b,*]

[a] School of Materials Science and Engineering, Chang'an University, Xi'an 710064, China
[b] Waikato Centre for Advanced Materials, School of Engineering, University of Waikato, Hamilton 3240, New Zealand

HIGHLIGHTS

- Short-time processing route is designed to produce cost-affordable and high-quality powder metallurgy titanium alloy.
- Rapid consolidation, one-step processing and fast heat treatment are applied to minimize the manufacturing cost and time.
- Superior strength-ductility combinations are achieved for the alloy after specific processing and fast heat treatment.
- The excellent mechanical properties are comparable to other expensive and time-consuming metastable β titanium alloys.

GRAPHICAL ABSTRACT

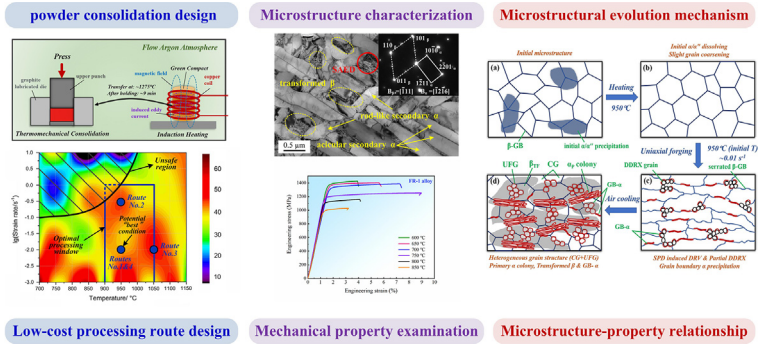

ARTICLE INFO

Article history:
Received 25 November 2020
Received in revised form 3 January 2021
Accepted 7 January 2021
Available online 09 January 2021

Keywords:
Cost-effective processing
Titanium alloy
Powder metallurgy
Microstructure evolution
Mechanical properties

ABSTRACT

Short-time processing route has been designed to manufacture cost-affordable and high-quality powder metallurgy (PM) metastable β titanium alloy, containing rapid powder consolidation (modified thermomechanical pressing), one-step thermomechanical processing (simple open die uniaxial hot forging by industrial press) and fast heat treatment (one-step annealing at various temperatures for only one hour). Based on comprehensive microstructure characterizations and mechanical property examinations, underlying microstructural evolution mechanism and microstructure-property relationship of the produced alloys were uncovered and elucidated thoroughly. Homogeneous macrostructure and fine-grain microstructure without undissolved particles and large pores are obtained for the alloy after thermomechanical powder consolidation as a result of the concurrent effect of external deformation and high-temperature diffusion. One-step open-die forging is verified to produce full-dense and sound PM alloy pancake with large-scale and high strength. Attributed to the harmonious concurrence of hierarchical α precipitation and heterogeneous grain structure, synergistic strength-ductility combinations are achieved for the alloy after specific processing and heat treatment with the tensile strength and strain at failure values of 1386.5 MPa/7.3% and 1252.3 MPa/9.0%, respectively. These strength-ductility combinations are comparable and/or even better than other metastable β titanium alloys prepared by some PM and ingot metallurgy approaches with relatively high cost and time consumption.

1. Introduction

Titanium and its alloys have become promising materials for advanced industries because of their balanced physical and mechanical

* Corresponding authors at: School of Materials Science and Engineering, Chang'an University, Xi'an 710064, China
E-mail addresses: zqy@chd.edu.cn (Q. Zhao), fei.yang@waikato.ac.nz (F. Yang).

https://doi.org/10.1016/j.matdes.2021.109457

properties, among which metastable beta titanium alloys are special ones to be attractive for aerospace and marine applications thanks to their outstanding performances including high specific strength, excellent corrosion resistance and wide service temperature range [1–3]. However, the applications of metastable beta titanium alloys are only confined within some specific fields like aircraft and military equipment, where the manufacturing cost is not a sensitive consideration [4,5]. The utilization of metastable beta titanium alloys can be expanded to other needed and crucial areas (automobile, civil, architecture and etc.) only when the cost is managed to be acceptable by simplifying hot processing, shortening manufacturing procedure and avoiding massive machining [6,7].

Powder metallurgy (PM) approaches have been regarded and applied as the feasible candidate to produce titanium parts with near-net shape forming and good quality against ingot metallurgy (IM) methods [8,9]. The initial idea for manufacturing titanium alloy products from powder is using the pre-alloyed (PA) powders to produce near-net-shape and high-performance parts, avoiding expensive processing and massive machining procedures (see the PA and IM route in Fig. 1), However, PA titanium alloy powders are usually expensive as they are produced from well-made alloy ingot and atomised by various energy-intensive and time-consuming techniques. Therefore, PA approaches are usually used for making near-net and complex-shaped components by some complicated ways, such as hot isostatic pressing (HIP) [10], metal injection moulding (MIM) [11] and additive manufacturing (AM) [12], and the products are required to have even better mechanical/physical performances than the IM counterparts without consideration of the cost. Different from PA approach, blended elemental (BE) approaches have been developed to make titanium alloy parts from powder mixture that consisted of pure titanium powder and other elemental/master-alloy powders. As the processes of melting/casting and atomization are avoided (see the BE routes in Fig. 1), the hydrogenation/dehydrogenation (HDH) titanium powder is much cheaper than PA powder [13]. Together with the near-net-shape forming feature, significant cost reduction of the titanium products can be achieved by the PM-BE approaches. The schematic diagrams showing the typical procedures of PM approaches are shown in Fig. 2.

The BE powder mixture is always pressed (to green compact) and then sintered in vacuum above β phase transformation temperature to homogenize the composition and consolidate the material to near-full dense (usually about 95% relative density). Vacuum sintering is usually utilized to consolidate the BE-PM titanium powder compacts to produce nearly full-dense titanium parts. Metastable β titanium alloys have been reported to be successfully prepared following this approach. Savvakin et al. [14] investigated the effect of iron contents on the microstructure and mechanical properties of the vacuum-sintered Ti-10V-xFe-3Al metastable β alloy. Similarly, the role of alloying element in the microstructural evolution during multiple-step vacuum-sintering of Ti-5Al-5Mo-5V-2Cr-1Fe (Ti-55521) metastable β alloy has been studied by Carman et al. [15]. Yang et al. [16] and Luo et al. [17] sintered Ti-1023 metastable β alloy and evaluated the mechanical performance of the consolidated alloy. Also, a series of quite comprehensive work was presented by Ahmed et al. [18–21] to establish the processing-microstructure-property relationships for Ti-55521, Ti-5Al-5Mo-5V-1Cr-1Fe (Ti-55511) and Ti-10V-3Fe-3Al (Ti-1033) metastable β alloys and their deformation behaviour are studied. It worth mentioning that it can take up to 10 h to sinter a batch of titanium compacts at the desired temperature from the start of heating to the completion of cooling the billets down to room temperature. These long-time processes lead to high energy consumption and low production efficiency during industrial manufacturing, which reduces the competitiveness of the BE-PM titanium products in term of their desired cost-effective nature.

Moreover, the as-sintered BE-PM titanium alloy parts usually have poor mechanical performance caused by high residual porosity and coarse microstructure. Many pieces of research have been conducted to eliminate the residual pores, adjust the microstructure and improve the mechanical properties of by using HIP and post-processing methods. Because HIP process is long-time taking and needs expensive equipment, then the thermomechanical processing (TMP) processes together

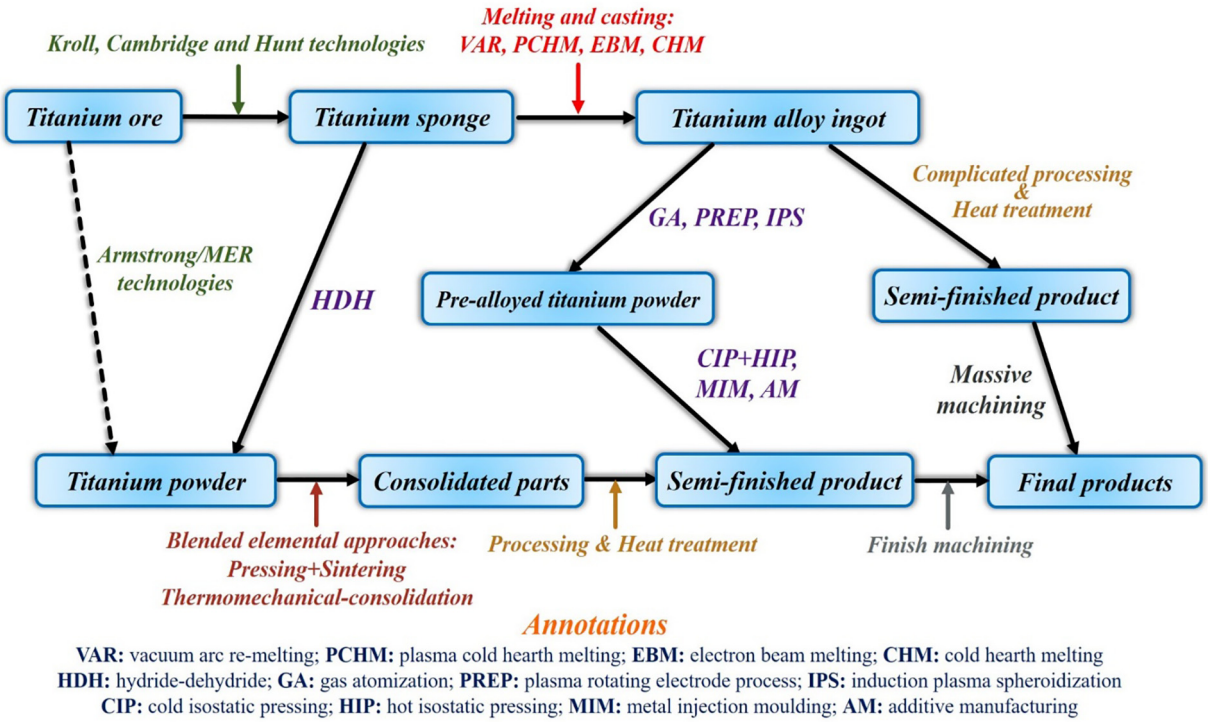

Fig. 1. Flow chart demonstrating conventional IM and common PM approaches for manufacturing titanium alloy products.

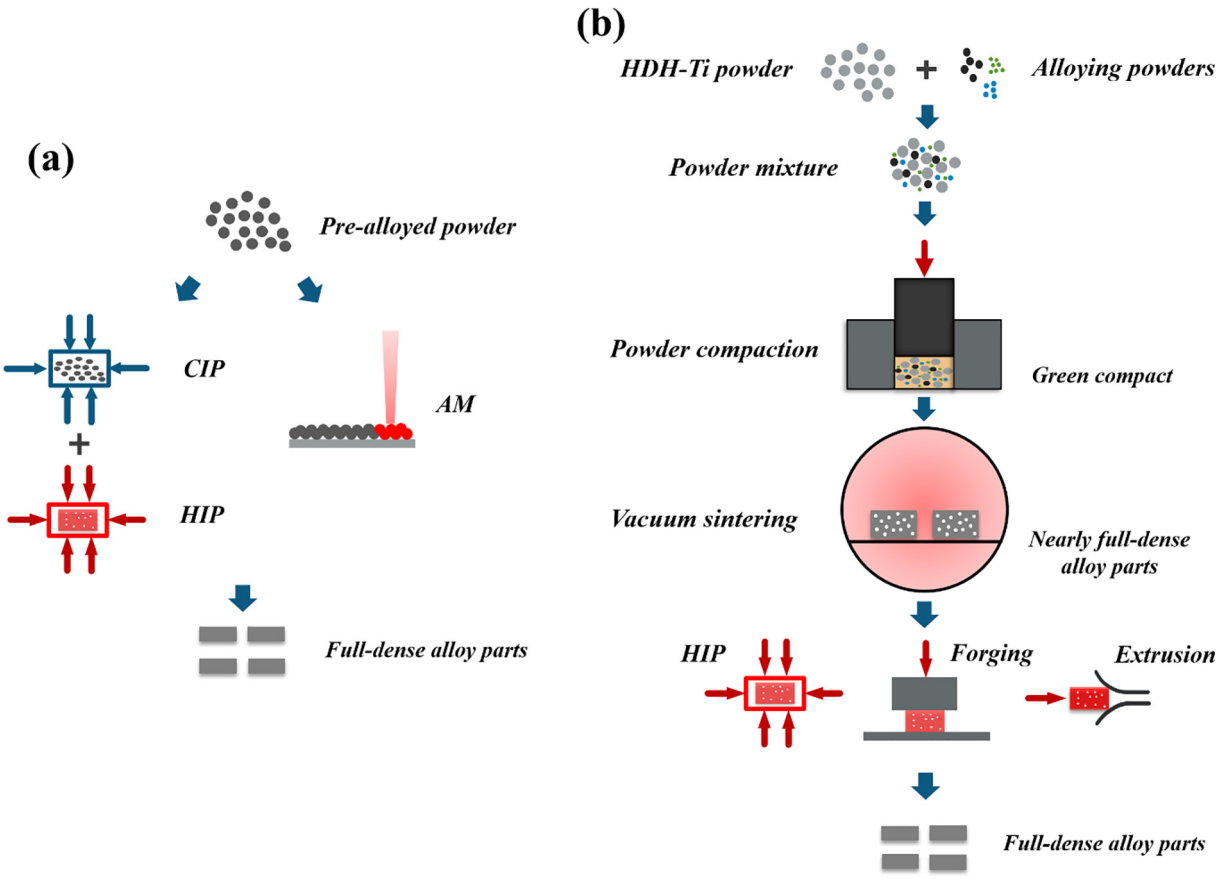

Fig. 2. Schematic diagrams showing typical procedures for two main PM titanium approaches: (a) pre-alloyed approach; (b) blended elemental approach.

with post-heat treatment are developed to produce BE-PM titanium alloy parts with wrought-like mechanical performance in a cost-effective way.

For the conventional metastable β titanium alloys, multiple-pass thermomechanical processing and complex heat treatment are always required to manipulate the microstructures and optimize the mechanical properties [22,23]. Thus, abundant researches have been done to investigate hot-processing optimization, deformation mechanism and resultant property enhancement for ingot metallurgy and PM-BE titanium alloys. Li et al. [24] employed deep neural network with isothermal deformation to optimize hot-working process for low-cost Ti-2Al-9.2Mo-2Fe alloy. Liu et al. [25] and Saboori et al. [26] studied the hot deformation behaviour of Ti-6Al-4V alloy prepared by CIP + sintering and AM (electron beam melting) in single-β phase field to optimize their hot processing, respectively. However, for the BE-PM titanium alloys, these complicated procedures are not a good choice anymore, as noticeable cost and time add-on. Because of fine-grain and high-oxygen level (higher β transus) peculiarities of PM alloys compared to the IM ones, an opportunity has been provided to design a relatively simple processing and treatment processes for BE-PM metastable β titanium alloys to minimize the manufacturing cost and time.

Nevertheless, there is still a lacking of systemic and comprehensive report focused on metastable β titanium alloys produced by cost-affordable BE-PM approach. Recently, a fast approach, thermomechanical powder consolidation (TPC), has been initiated to consolidate metastable beta titanium alloy parts cost-effectively from powder mixture instead of vacuum sintering [27]. In this work, based on our preliminary study, simple thermomechanical processing route and fast heat treatment have been optimized and employed for a typical commercialized metastable β titanium alloy (Ti-5553) to reform the microstructure and improve the mechanical properties of the consolidated parts after TPC. With the combination of various characterization techniques and in-depth analysis, the microstructural evolution mechanism and underlying microstructure-property relationship are revealed and disclosed. At last, the limitation and perspective of this current work are also provided and discussed.

2. Experimental details

2.1. Thermomechanical powder consolidation

The PM Ti-5553 alloy in this study was synthesized from a powder mixture with the nominal composition of Ti-5Al-5Mo-5 V-3Cr (wt%) prepared from elemental powders of hydride-dehydrided (HDH) titanium powder (−200 mesh, 99.6%), Al powder (−200 mesh, 99.9%), Al35-V65, Al15-Mo85 and Al30-Cr70 (wt%) master alloy powders (−75 μm, commercial purity). The choice of these raw powders was based on their cost-effective nature, small size and irregular surface morphology (except the spherical Al powder) which makes them favourable to be compacted and consolidated during warm compaction and TPC.

The alloy was consolidated from the raw powders through the processes of powder mixing, warm compaction and TPC. The schematic diagram showing this preparation route is exhibited in Fig. 3. The raw powders were first weighted (500 g) to make the nominal composition of Ti-5Al-5Mo-5V-3Cr (wt%). Afterwards, a V-shaped blender was used to mix the powders into homogeneous mixture at a rotation rate of 60 rpm for 90 min. The powder mixture was then warm-compacted into green compact (relative density about 84%) using a graphite

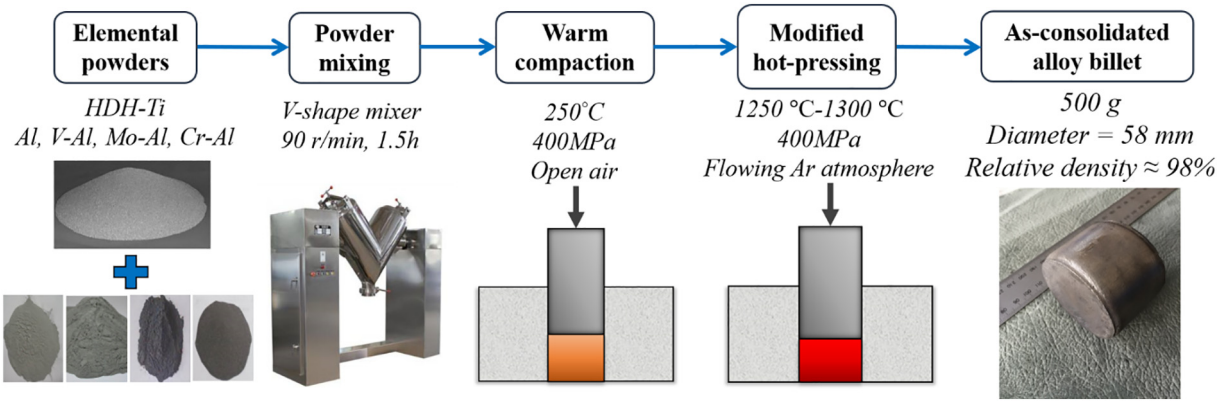

Fig. 3. Schematic diagram showing the preparation route for as-consolidated PM Ti-5553 alloy.

lubricated die (cylinder shape, a diameter of 56 mm) at the temperature about 250 °C and a uniaxial pressure about 400 MPa in air.

TPC of the green compact was achieved by modified hot pressing, performed using a 100-ton oil hydraulic press equipped with a glove chamber. The green compact was firstly inductive-heated to the target temperature about 1275 °C with a very high heating rate up to 200 °C/min. The rapid-inductive heating of the green powder compact was enabled by the copper induction coil and the external high-frequency power supply. The induction coil carries an alternating current, which creates a magnetic field that induces an eddy current in the conductive metal powder compact to produce a strong thermal effect. After holding at the temperature for about 9 min, the hot compact was transferred into a slightly larger graphite lubricated die (cylinder shape, the diameter is 58 mm), followed by uniaxial hot pressing to consolidate the alloy billet thermomechanically. Flowing argon atmosphere was applied to the chamber during heating, pressing and cooling processes to control the oxygen level (below 200 ppm) for the elimination of serious oxidation.

More detailed induction heating mechanism and the experimental set-up can be found in the sketch exhibited in Fig. 4. It was examined that the overall processing time is only about 16–17 min with very low electricity consumption of about 1.6 kW·h per compact. Consequently, the developed TPC approach has been proved to reduce the consolidation cost and time effectively, compared to the widely-utilized vacuum sintering method. The relative density of the as-consolidated alloy was determined to be about 98%, and its chemical composition was measured as Ti-4.99Al-4.94V-4.94Mo-2.90Cr-0.36O-0.0021N.

2.2. Thermomechanical processing and heat treatment

Based on the understanding of hot deformation behaviour, processing maps and microstructural evolution characteristics obtained from our preliminary work [28], the thermomechanical processing conditions were designed for the as-consolidated PM Ti-5553 alloy billets, then the determined one-step open-die forging was performed at different conditions (temperatures, strain rates and cooling modes) to produce large-size alloy pancakes (as-forged) with low cost and reduced time consumption.

The optimal processing window of the alloy was suggested as: the deformation temperature between 900 °C–1050 °C, the strain rate below 1 s^{-1}, and the deformation degree is higher than 70% of height reduction. The PM Ti-5553 alloy exhibited excellent hot workability with stable flow and satisfied microstructure control within this processing window. Furthermore, the condition of 950 °C/0.01 s^{-1} could be the potential "best" processing region, as the occurrence of extensive dynamic recrystallization (DRX) with significant grain refinement (the results of isothermal compression microstructure). Therefore, four simple one-step TMP routes (for the comparisons of processing temperature, strain rate and cooling mode) were finally selected for processing the as-consolidated PM Ti-5553 alloy billets based on the constructed power dissipation map (the results of isothermal compression testing), as shown in Fig. 5.

The as-consolidated PM alloy billets (after TPC) were thermomechanical processed (single uniaxial open-die hot forging) at elevated temperatures using a 650-ton industrial-scale hydraulic quick-forging press (Northwest Institute of Nonferrous Metal Research, China). As shown in Fig. 6, the billets were heated up to 950 °C/1050 °C and held the temperature for 30 min. After the hot billets were transferred to the pre-heated (500 °C) working platform of the 650-ton press, they were subsequently forged into alloy pancakes at different strain rates and with a large deformation degree of 75% height reduction, and then cooled down to room temperature with different cooling modes. The alloys produced following different routes are referred as to FR-1,

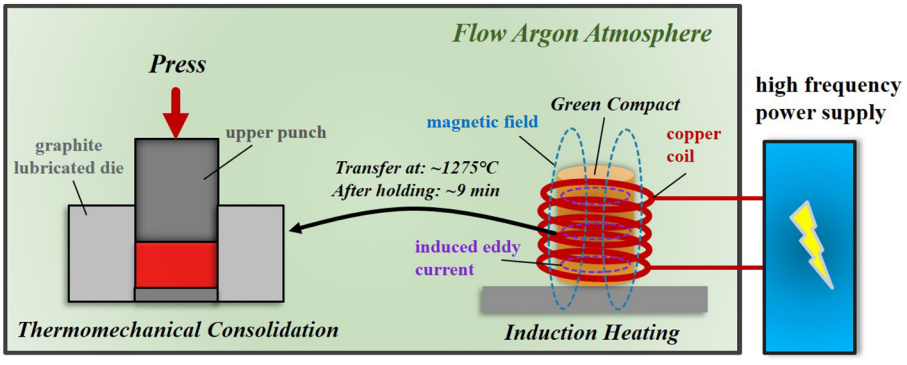

Fig. 4. Schematic diagram showing the mechanism and the experimental set-up of the developed thermomechanical powder consolidation (TPC) approach.

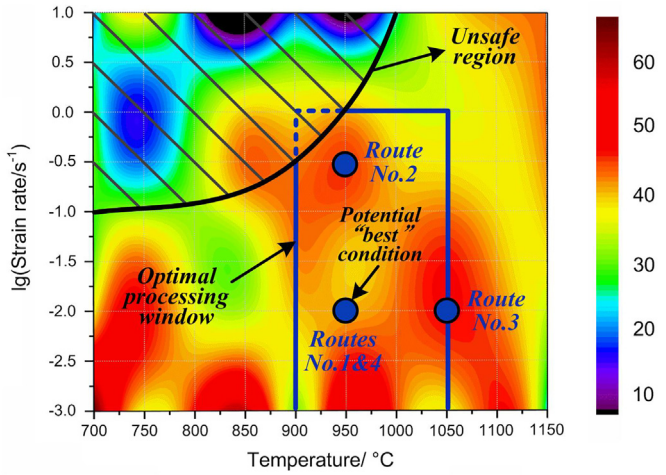

Fig. 5. The indications of applied TMP conditions on the power dissipation map (ε=1.0, constructed based on Ref. [28]).

FR-2, FR-3 and FR-4, respectively. Fast heat treatment was conducted in a muffle furnace, the treatment temperatures were set as 600 °C to 850 °C (interval of 50 °C), and the temperature was held for only 1 h, followed by air cooling. Microstructure characterizations, mechanical property examinations and heat treatment were conducted using the material from the middle areas of the alloy pancakes to avoid the deformation dead zone.

2.3. Material characterizations

The as-consolidated billet was wire-cut along the cross-section direction and then the surface was precisely machined. Afterwards, the cross-section surface was etched directly and uniformly in a modified Kroll's reagent containing 10 vol% HF, 20 vol% HNO_3 and 70 vol% H_2O to reveal the macrostructure of the billet. Optical microscopy (OM, OLYMPUS-PMG3), scanning electron microscopy (SEM, JSM-6460 and Hitachi-S4700), spherical aberration corrected transmission electron microscopy (ACTEM, JEM-ARM200F) and transmission electron microscopy (TEM, JEM-2100) were used to examine the microstructures of the alloy samples. The samples for OM and SEM microstructure observations were firstly ground (SiC paper) and mechanical polished (silica gel) to reach mirror-surface finish followed by etching (aforementioned modified Kroll's reagent) to uncover the microstructure. For TEM sample preparation, small alloy disks with a diameter of 3 mm were first ground down to 60 μm in thickness, and then ion-beam milled for examination.

X-ray diffraction (XRD) analyses were performed on a D8 Advance X-ray diffractometer (Bruker Ltd., USA) equipped with a Cu Kα radiation source ($\lambda = 0.154157$ nm) to determine the phase constitutions of the processed alloys. Dog-bone shaped tensile specimens with a gauge section of 20 mm × 2 mm × 2 mm were prepared (electric discharge machining and surface grinding) from the alloys at various conditions. Then, room temperature tensile testing was conducted on a universal testing machine (Instron-4204) at a strain rate of 10^{-4} s^{-1}, following the standard of ASTM E8/E8M-16ae1 (for P/M metallic materials). After tensile testing, the fractographic features were characterized by SEM (JSM-6460). At least three specimens were tested during the tensile testing at each condition for experimental accuracy and reliability. Hardness measurements were conducted using a microhardness tester (FM-700, Leco Ltd.) with a diamond right-square-pyramid indenter having the taper angle of 136°, following the standard of ASTM E92–17 (Vickers Hardness). The load was pressurized for 10 s for the test, and the measurements were repeated 10 times to obtain the averaged behaviour of the sample.

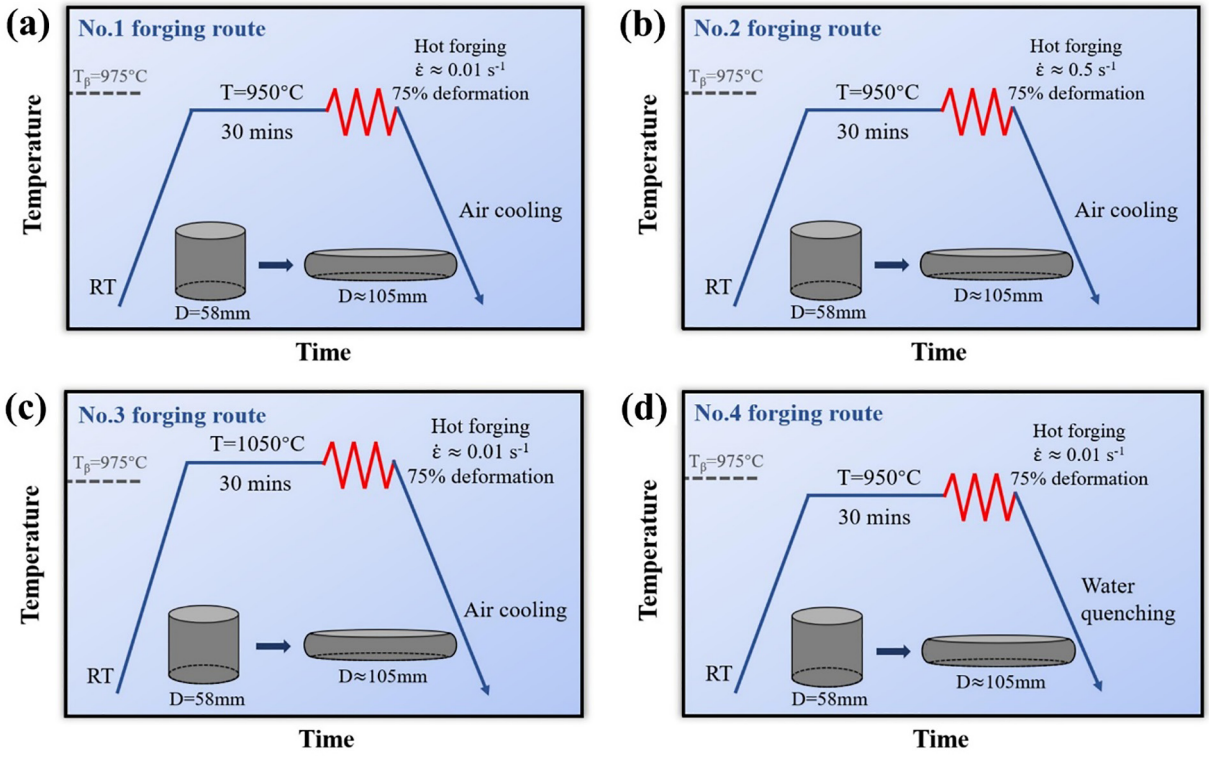

Fig. 6. Schematic diagrams showing various simple thermomechanical processing routes for the as-consolidated Ti-5553 alloy billets: (a) forging route No.1; (b) forging route No.2; (c) forging route No.3; (d) forging route No.4. The strain rate is controlled approximately at the designed values.

3. Results

3.1. Initial macrostructure and microstructure of as-consolidated alloy

The macrostructure photo and optical microstructure images of the as-consolidated alloy billet are shown in Fig. 7. As shown in Fig. 7a, the cross-section macrostructure of the alloy billet is homogeneous and there are no undissolved master-alloy powder particles. The reason why the TPC approach can well consolidate titanium alloy compacts in such a short time is the concurrent effect of external deformation and high-temperature diffusion. This effect makes it possible for elemental powder particles to be completely dissolved in the matrix rapidly due to the increases of diffusion rate and particle's movability. On the contrary, a longer time is required for particle dissolving and densifying in the pressure-less vacuum sintering approach.

Fig. 7b-c shows the initial microstructures of the as-consolidated PM Ti-5553 alloy. It can be seen that the thermomechanical-consolidated alloy consists of primary equiaxed β phase, with an average grain size of about 100 μm, and the precipitation phase areas are distributed within β grain matrix or near β grain boundaries. Moreover, it has been proved that the precipitation is composed of acicular α and lath α″ phases which are responsible for the early fracture of the as-consolidated alloy [29]. It is also worth mentioning that some residual pores are visible in the microstructure, but their amount (less than 2%) and size (less than 2 μm) are very limited.

3.2. Microstructure of the processed alloy

Figs. 8 and 9 show the OM and SEM microstructures of the as-forged alloys processed following the designed one-step forging routes, respectively. Overall, the microstructure characteristics, including grain size/structure, precipitation proportion/distribution and phase morphology of the processed alloys, are highly depended on the processing conditions.

As shown in Fig. 8a-c, FR-1 alloy possesses a heterogeneous grain structure that is composed of slightly elongated coarse grains (CG) and near-equiaxed ultra-fine grains (UFG). The CG has an average grain size of 100–250 μm, while the average grain size for UFG is only about 10–20 μm. Furthermore, two types of α phases are observed, including primary α phase (α_p) colony and very fine α phase in transformed β structure (β_{TF}). Additionally, there is also a large proportion of β grains in the microstructure without α precipitation. SEM observation (Fig. 9a-c) suggests that the UFG primarily contains β_{TF} structure surrounded by continuous grain boundary α phase (GB-α), while the CG is mainly precipitation-free β phase (matrix). The α_p colonies are located near β grain boundaries (Fig. 8b and Fig. 9b), especially the boundaries of UFG. β_{TF} can also be found between the lath α_p phases (Fig. 9c), showing a large amount of fine α precipitates on residual β phase. The detailed microstructural variation mechanisms and beneficials for this harmoniously-combined microstructure will be discussed later.

For FR-2 alloy, as shown in Fig. 8d-f, the microstructure is composed of precipitation bands and β phase matrix. The precipitation bands and β phase matrix are alternately distributed, with the dominance of precipitation bands. Moreover, there is no large-sized α_p and grain boundary (GB) invisible in the microstructure. In the corresponding SEM images (Fig. 9d-f), large prior β grains are still at the severely-elongated stage with serrated GBs. The precipitation bands are observed to be made up of widespread β_{TF} structures that have small-sized acicular α phase and residual β phase distributed between the aforementioned acicular α phases. The acicular α phases in β_{TF} structure of FR-2 alloy are much coarser than those in FR-1 alloy but the size distribution is nearly homogeneous.

The microstructure of FR-3 alloy shows entirely different features comparing to FR-1 and FR-2 alloys. As shown in Fig. 8g-i, the prior β grain of FR-3 alloy has near-equiaxed shape (Fig. 8g) and its grain size is obviously coarser than that of FR-1 alloy, with an average grain size higher than 300 μm. Dispersive α precipitates are observed besides several isolated precipitate-free β phase, and some α_p phases are appeared at β-GB and in the inside of the prior β grain. Fig. 9g-i shows that lath and fibrous-shaped α_p is distributed along the prior β-GB, forming long GB-α phases, while some α_p phases locate inside the prior β grain are present as short rod-like shape. It is uncovered that the widespread precipitation area in FR-3 alloy (Fig. 9i) is also in the form of β_{TF} structure, which is very similar to the β_{TF} structure showed in FR-1 alloy (Fig. 9c).

Fig. 8j-l shows the microstructure of FR-4 alloy, and obvious rapid-cooling features are clearly observed. The β grains are elongated along the horizontal direction with serrated GB, and some small equiaxed grains are distributed along and/or near the prior β-GB with more prominent boundaries (Fig. 8l). These observation results indicate that both dynamic recovery (DRV) and partial discontinuous dynamic recrystallization (DDRX) take their effects during the forging processes of the alloy following routes No.1 and No.4 (at the potential "best" TMP condition shown in Fig. 5). SEM images (Fig. 9j-l) reveal that the newly-formed DDRX grains with a size of 5–10 μm are dressed by fine α precipitates at their boundaries. Furthermore, some fine α precipitates are also observed at the serrated β-GB. The existence of continuous GB-α phase in FR-4 alloy is further confirmed by TEM observation (see Fig. 10). These observation results suggest that these fine GB-α phases along the boundaries of DDRX grains and prior β grains are formed dynamically as the precipitations from β matrix during the forging processes are attributed to the concurrent effect of external deformation and thermal activation. Furthermore, there is no β_{TF} structure appeared in the water-quenched FR-4 alloy, which further demonstrates that the β_{TF} structure in FR-1, FR-2 and FR-3 alloys are formed during air cooling process (much slower cooling rate comparing to rapid water-quenching). At last, there are no obvious and visible residual pores

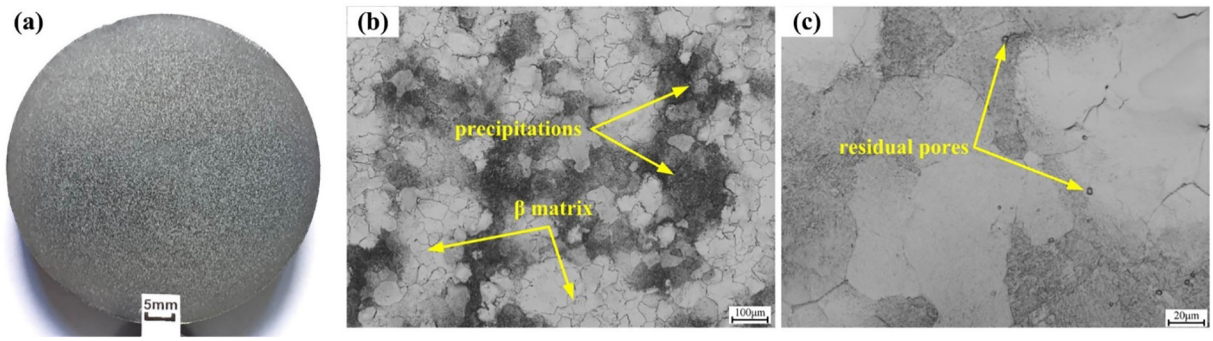

Fig. 7. Macrostructure and microstructure images of as-consolidated alloy billet: (a) cross-section macrostructure; (b)-(c) optical microstructures.

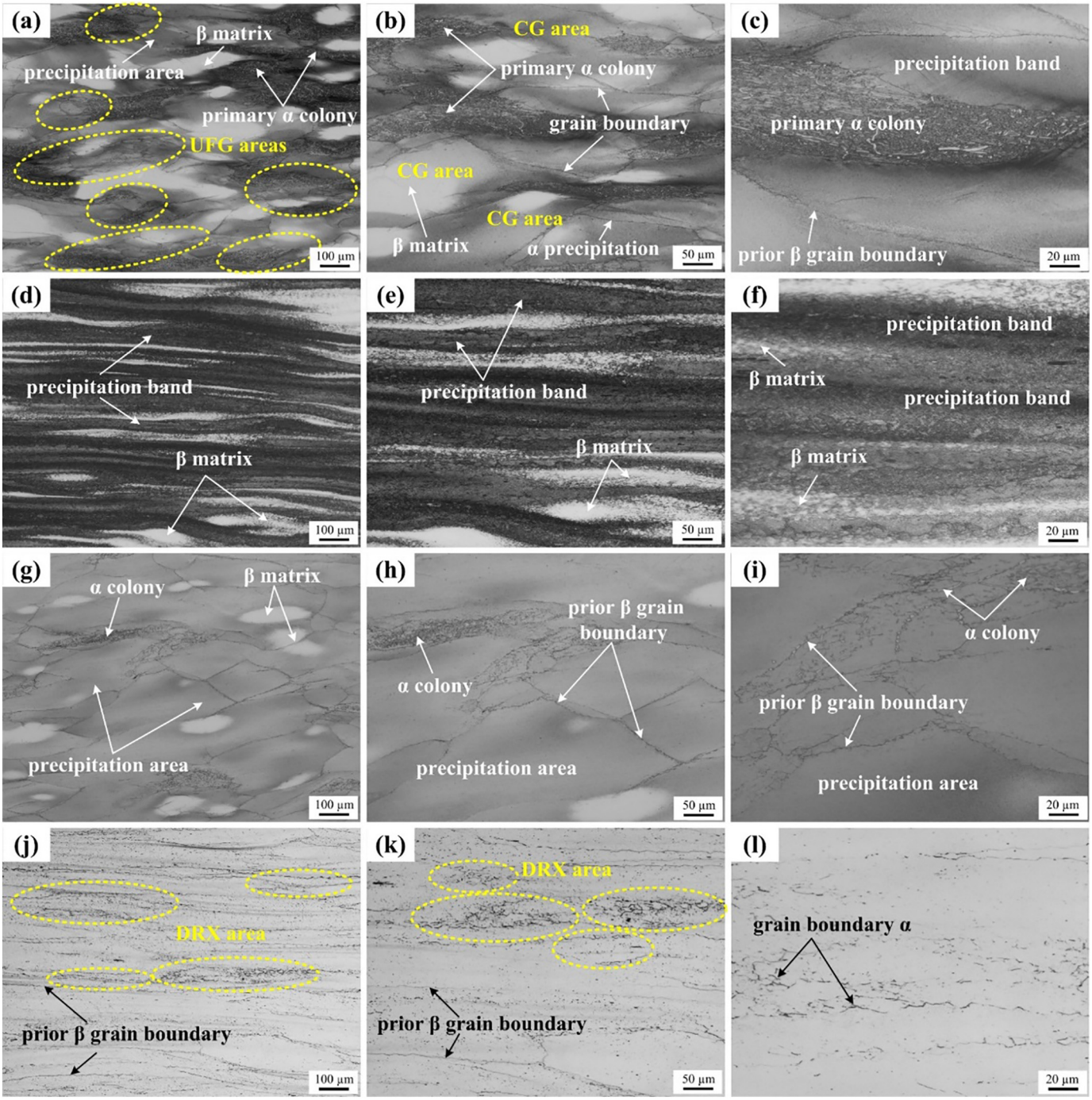

Fig. 8. Optical microstructures of as-forged PM Ti-5553 alloy pancakes processed via various routes: (a)-(c) FR-1 alloy; (d)-(f) FR-2 alloy; (g)-(i) FR-3 alloy; (j)-(l) FR-4 alloy. Forging was performed along the vertical direction.

observed in the microstructures of all the alloys processed following various TMP routes. These results prove that the 2% residual micropores in the alloy at as-consolidated stage have been completely eliminated after TMP.

XRD patterns of the as-forged PM Ti-5553 alloys at different conditions are presented in Fig. 11. It suggests that the peaks of α and β are indexed in all forged alloys (FR-1, FR-2, FR-3 and FR-4). Moreover, FR-1 alloy has the highest α peak intensity, while the number of α peaks and their intensities becomes significantly less and lower in FR-4 alloy with stronger β peaks, comparing to other alloys. FR-1, FR-2 and FR-3 alloys have extensive α_p and/or fine α precipitation in β_{TF} structures, leading to the strong indexed α peaks in the XRD patterns. On the contrary, only a limited proportion of fine α precipitation located along GBs is found in FR-4 alloy, resulting in weak α peaks to appear on its XRD pattern.

3.3. Mechanical properties of the consolidated and processed alloys

Fig. 12 shows the typical room-temperature tensile curves of the as-consolidated PM Ti-5553 alloy and as-forged alloys processed following

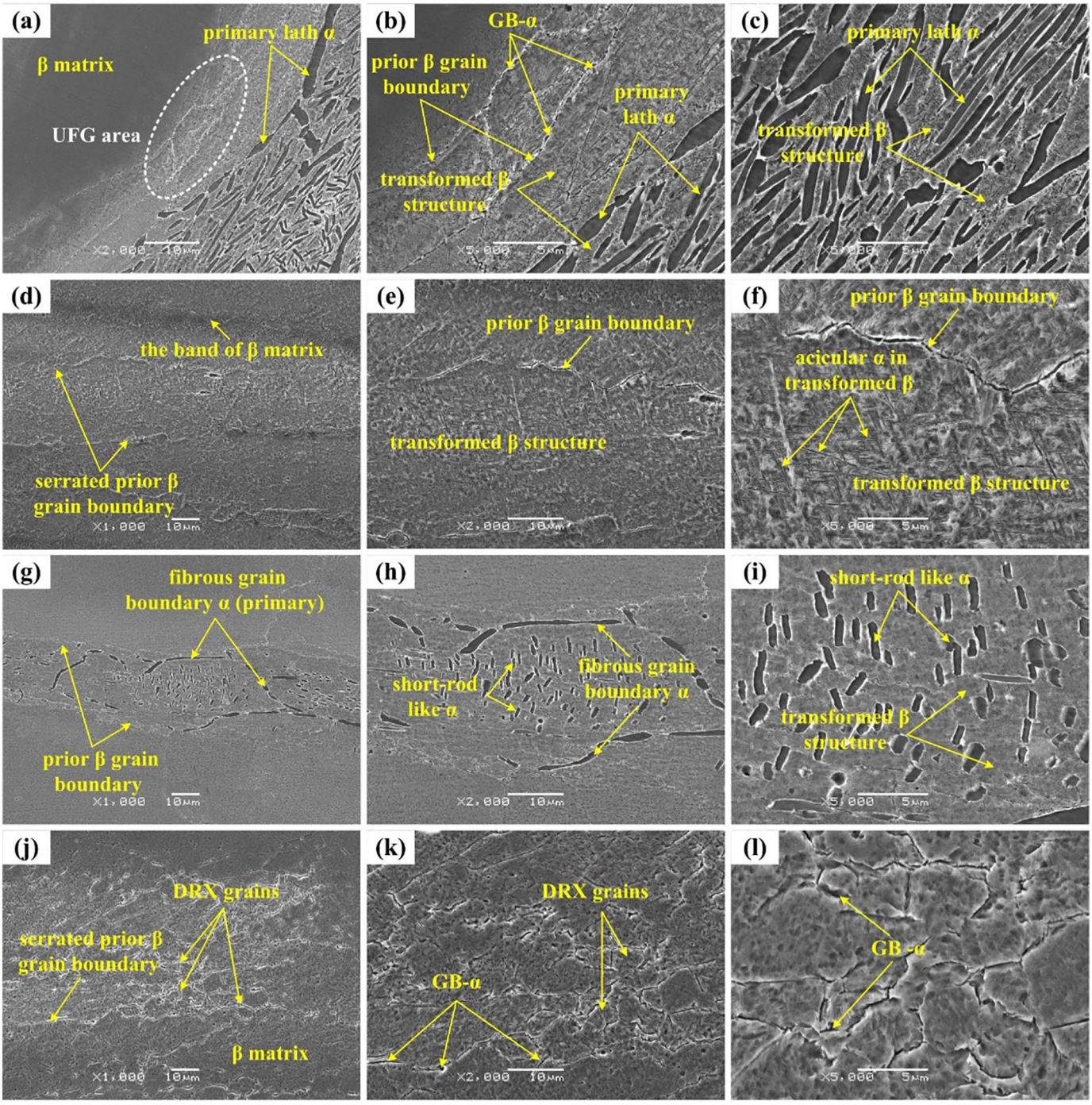

Fig. 9. SEM microstructures of as-forged PM Ti-5553 alloy pancakes processed via various routes: (a)-(c) FR-1 alloy; (d)-(f) FR-2 alloy; (g)-(i) FR-3 alloy; (j)-(l) FR-4 alloy. Forging was performed along the vertical direction.

different TMP routes, and the detailed tensile properties are shown in Table 1, together with the micro-hardness testing results.

Overall, it is apparent that the strength and hardness of PM Ti-5553 alloy are increased significantly by TMP, with values of yield stress (YS), ultimate tensile stress (UTS) and microhardness (MH) increased from 852.5 MPa, 912.6 MPa and 357.2 HV (as-consolidated stage) to 1152.3 MPa–1374.3 MPa, 1193.2 MPa–1450.9 MPa and 394.2 HV–492.4 HV (as-forged stage), respectively. Moreover, the designed forging routes also help to improve the ductility for FR-1 and FR-2 alloys, with the slightly increased strain at failure (ε_f) from 2.4% (as-consolidated stage) to 3.8% and 2.5% (as-forged stage), but the ductility is even decreased for the FR-3 alloy and FR-4 alloy after forging (only 2.0% and 1.8%).

Fig. 13 shows the typical tensile fracture surface morphology of the as-forged PM Ti-5553 alloys. Small cleavage facets having river-like patterns and tear ridges around are observed in FR-1 alloy (Fig. 13a-b). Meanwhile, there is a large number of small dimples distributed randomly on the fracture surface, meaning that the alloy was plastically deformed to some extent during the tensile test. These above observations indicate that the fracture of FR-1 alloy is dominated by ductile-brittle mixed mechanism. It can be seen in Fig. 13c-d that the fracture surface of FR-2 alloy has large cleavage facets featured by river-like patterns

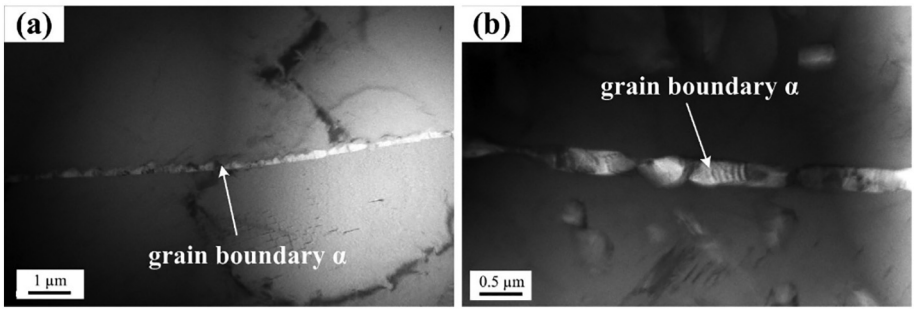

Fig. 10. TEM images showing the morphology of grain boundary α phases in FR-4 alloy.

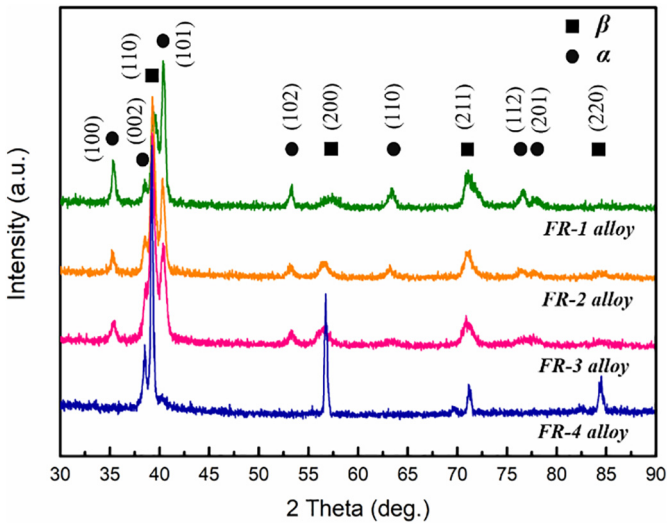

Fig. 11. XRD patterns of as-forged PM Ti-5553 alloys processed following different routes.

and tear ridges. Moreover, dimples and intergranular fracture characteristics are also observed, but the amount and size of the dimples are much less and smaller than those of FR-1 alloy. Thus, it can be inferred that FR-2 alloy is fractured by brittle cleavage mechanism with the

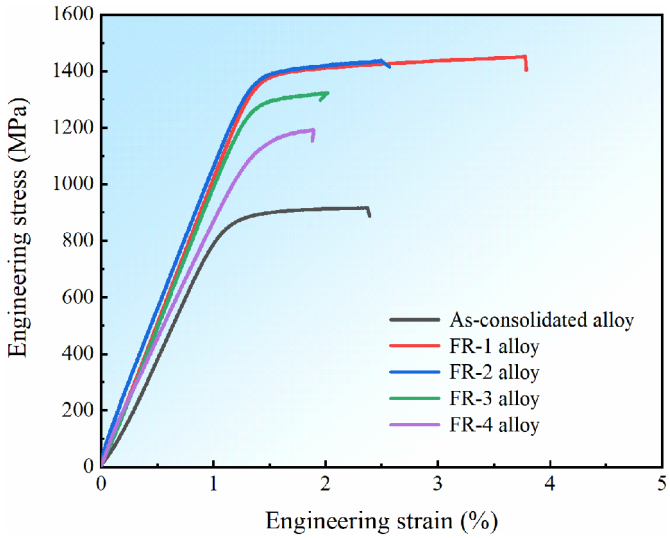

Fig. 12. Typical tensile curves for the as-consolidated and processed alloys.

Table 1
Mechanical properties for the as-consolidated and processed alloys.

Alloy condition	Yield stress[a] (YS/MPa)	Ultimate tensile stress (UTS/MPa)	Strain at failure (ε_f/%)	Microhardness (MH/HV)
As-consolidated	852.5	912.6	2.4	357.2
FR-1 alloy	1374.3	1450.9	3.8	492.4
FR-2 alloy	1333.8	1434.2	2.5	469.8
FR-3 alloy	1292.6	1316.5	2.0	421.7
FR-4 alloy	1152.3	1193.2	1.8	394.2

[a] Yield point is set at 0.2% plastic strain.

combination of intergranular and transgranular features, and the plastic deformation degree was low during the tensile test.

As shown in Fig. 13e-f, a near-flat fracture surface is observed for the specimen of FR-3 alloy, with the appearance of cleavage facets and tear ridges. Besides, dimples are almost disappeared from the fracture surface, which illustrates that the brittle transgranular cleavage mechanism dominates the fracture of FR-3 alloy. Completely different failure characteristics are observed in the fracture surface for FR-4 alloy (Fig. 13g-h), including a very flat and smooth cleavage facture surface without other obvious features. These results mean that the fracture behaviour of FR-4 alloy is complete brittle cleavage mechanism with no plastic deformation. The abovementioned fracture surface morphologies and fracture mechanisms of the as-forged alloys comply well with the tensile ductility results. There is a continuous deterioration tendency of the ductility from FR-1 to FR-4 alloy (FR-1 alloy shows the highest ductility, while FR-4 alloy has the lowest one among the as-forged alloys), corresponding to the fracture mode varies from mixed ductile-brittle fracture to complete brittle fracture.

3.4. Microstructure of the heat-treated alloy

Although the PM Ti-5553 alloys processed following various forging routes show enhanced mechanical properties comparing to that of the as-consolidated alloy, their ductility, with the ε_f values of 1.8%–3.8%, are still not acceptable for practical engineering applications. Therefore, post-heat treatments become a necessity to be performed for the as-forged alloys to reform their microstructure and improve the ductility, without significant sacrifice in their strength. Only FR-1 alloy (has the highest mechanical properties among the forged alloys) and FR-4 alloy (the microstructure can be significantly changed since the alloy is supersaturated after water quenching) were selected for further investigating of the heat treatment effects on the alloys' microstructure and mechanical properties.

Fig. 14 shows the SEM microstructures of heat-treated FR-1 alloy. As shown in Fig. 14a_1-b_5, FR-1 alloy heat-treated at 600 °C and 650 °C has microstructures containing heterogeneous grain and hierarchical phase (tri-modal) structures. Both prior β-CG and β-UFG are observed

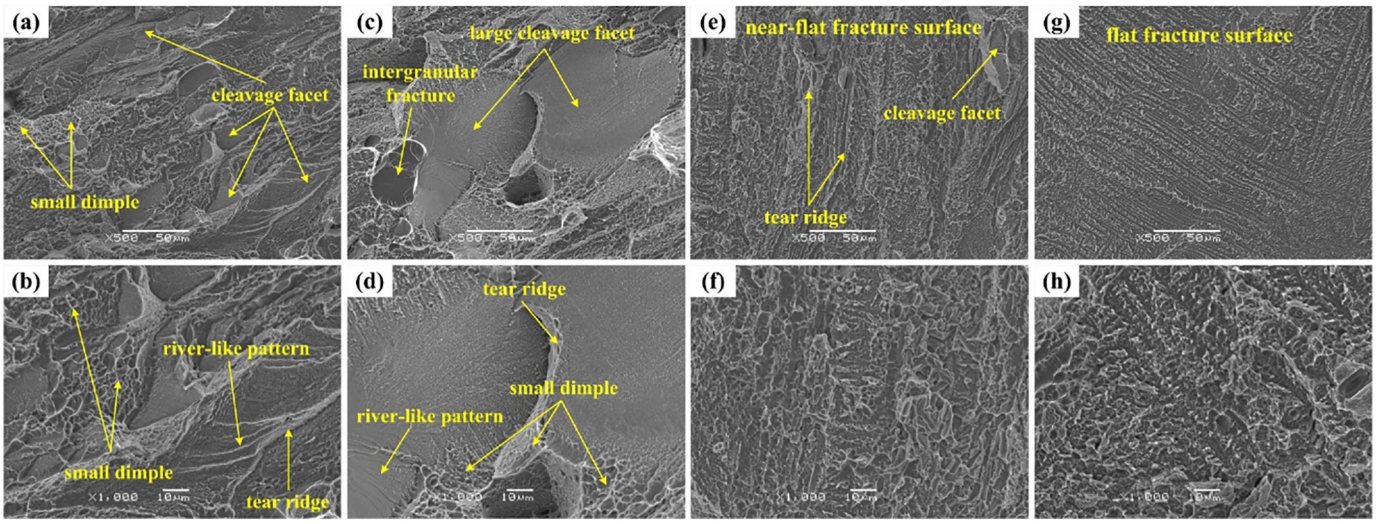

Fig. 13. Representative SEM fracture surfaces of the as-forged PM Ti-5553 alloy pancakes after tensile testing: (a)-(b) FR-1 alloy; (c)-(d) FR-2 alloy; (e)-(f) FR-3 alloy; (g)-(h) FR-4 alloy.

in the microstructure. Meanwhile, it can be observed that multiple α precipitation hierarchy of the alloy heat-treated at these conditions is composed of α_p colony, GB-α, acicular secondary α phase (α_s) and β_{TF} structure. Similar microstructures are obtained for the FR-1 alloy heat-treated at 700 °C and 750 °C to those of the alloy treated at 600 °C and 650 °C, as shown in Fig. 14 c_1-d_5, except that some acicular-shaped α_s phases grow coarse and become thick acicular, rod-like and spherical shapes. Furthermore, with increasing the heat treatment temperature from 600 °C to 750 °C, more rod-like and spherical α_s phases are observed than acicular α_s phases.

AC-TEM images (see Fig. 15) show the detailed microstructure of FR-1 alloy heat-treated at 700 °C. The α precipitations exhibit clear tri-hierarchical features composed of large-sized lath α_p (verified by the SAED pattern in Fig. 15b), fine acicular/rod-like α_s and nanoscale needle-like tertiary α (α_t, located inside of β_{TF} structure). The co-existence of α_t and β phase inside the β_{TF} structure is further confirmed by the SAED pattern in Fig. 15c. Dispersed acicular/rod-like α_s phases are distributed randomly in the microstructure with various directions, and β_{TF} structure is distributed between lath α_p and α_s phases. Meanwhile, the dislocation density is very low in the microstructure, which means the residual stress of FR-1 alloy is almost eliminated by static recovery and the alloy's microstructure stability is significantly improved after heat treatment at 700 °C.

When increasing the heat treatment temperature to relatively high temperatures of 800 °C and 850 °C, the microstructures of heat-treated FR-1 alloy become markedly different comparing to the alloy heat-treated at 600 °C–750 °C, as shown in Fig. 14e_1-f_5. The prior β-UFG structure showed in the forged alloy is disappeared, coarse α_s phases with rod-like and spherical shapes are visible, and the lath α_p phases show obvious coarsening and spheroidization tendency. Furthermore, there are some precipitation-free areas composed of only β phase. Fig. 16 shows the detailed TEM microstructure of FR-1 alloy heat-treated at 850 °C. It is apparent that only coarsened α_s phases (rod-like and spherical shapes, confirmed by the SAED pattern in Fig. 16b) and β matrix are observed and no β_{TF} structures, α_t phases, dislocations are visible.

Fig. 17 shows the SEM images of FR-4 alloy heat-treated at different temperatures. It can be observed that primary α_p colonies appear in the microstructures of all heat-treated alloys. The width of α_p colonies (about 10 μm) is smaller in the heat-treated FR-4 alloy than that in the heat-treated FR-1 alloy (larger than 30 μm), although the α_p lath has similar morphology. Similar to FR-1 alloy, FR-4 alloy also possesses a heterogeneous grain structure (CG and UFG) with multi-hierarchical α precipitation (lath α_p, acicular/rod-like/spherical α_s, nanoscale needle-like α_t within β_{TF} structure and GB-α) features when the heat treatment is conducted at the temperatures between 600 °C and 750 °C (see Fig. 17a_1-d_3).

With increasing the heat treatment temperature to 800 °C and 850 °C (see Fig. 17e_1-f_3), FR-4 alloy exhibits a simplex microstructure having rod-like/spherical α_s precipitation and spheroidizing lath α_p phases on the β matrix. It is also noticed that the size of α_s phases and the spheroidization/growth tendency of α_s and α_p are larger and more serious in FR-4 alloy than those in FR-1 alloy when the alloys are heat-treated at an identical temperature (800 °C and 850 °C).

3.5. Mechanical properties of the heat-treated alloys

Representative room-temperature tensile curves of the FR-1 and FR-4 alloys heat-treated at different temperatures are exhibited in Fig. 18. Moreover, their detailed tensile properties are listed in Tables 2 and 3, respectively, together with the hardness measurement results. By comparing the testing results of the as-processed and heat-treated alloys, it is clear that the mechanical properties of as-forged alloys have been balanced/improved or deteriorated/reduced by the designed fast heat treatment depending on the specific treatment temperature.

For FR-1 alloy (see Fig. 18a and Table 2), when it is heat-treated at the temperatures between 600 °C and 750 °C, the heat-treated alloy's ductility has been significantly improved compared to those of as-forged stage. Specifically, the ductility is continually improved with increasing the heat treatment temperature, showing a value of 4.0% for the 600 °C-treated one and 9.0% for the 750 °C-treated one. Showing the reverse tendency, the corresponding strength/hardness of the heat-treated FR-1 alloy is slightly and gradually reduced comparing to those of as-forged stage, having the UTS of 1420.2 MPa and hardness of 488.6 HV for the 600 °C-treated one, and the UTS of 1252.3 MPa and hardness of 410.2 HV for the 750 °C-treated one. Particularly, two excellent strength-ductility combinations are successfully achieved for FR-1 alloy heat-treated at 700 °C and 750 °C, with values of 1386.5 MPa/7.3% and 1252.3 MPa/9.0%, respectively. These strength-ductility balances are not only acceptable and qualified for metastable β titanium alloys in engineering applications but also be comparable to or even better than those of the metastable β titanium alloys (including Ti-5553 alloys) manufactured by other PM methods [30–33] and IM counterparts [2,34,35], as demonstrated in Fig. 19. Nevertheless, both the ductility and strength/hardness are lowered severely for the 800 °C and 850 °C heat-treated FR-1 alloy than those of as-forged

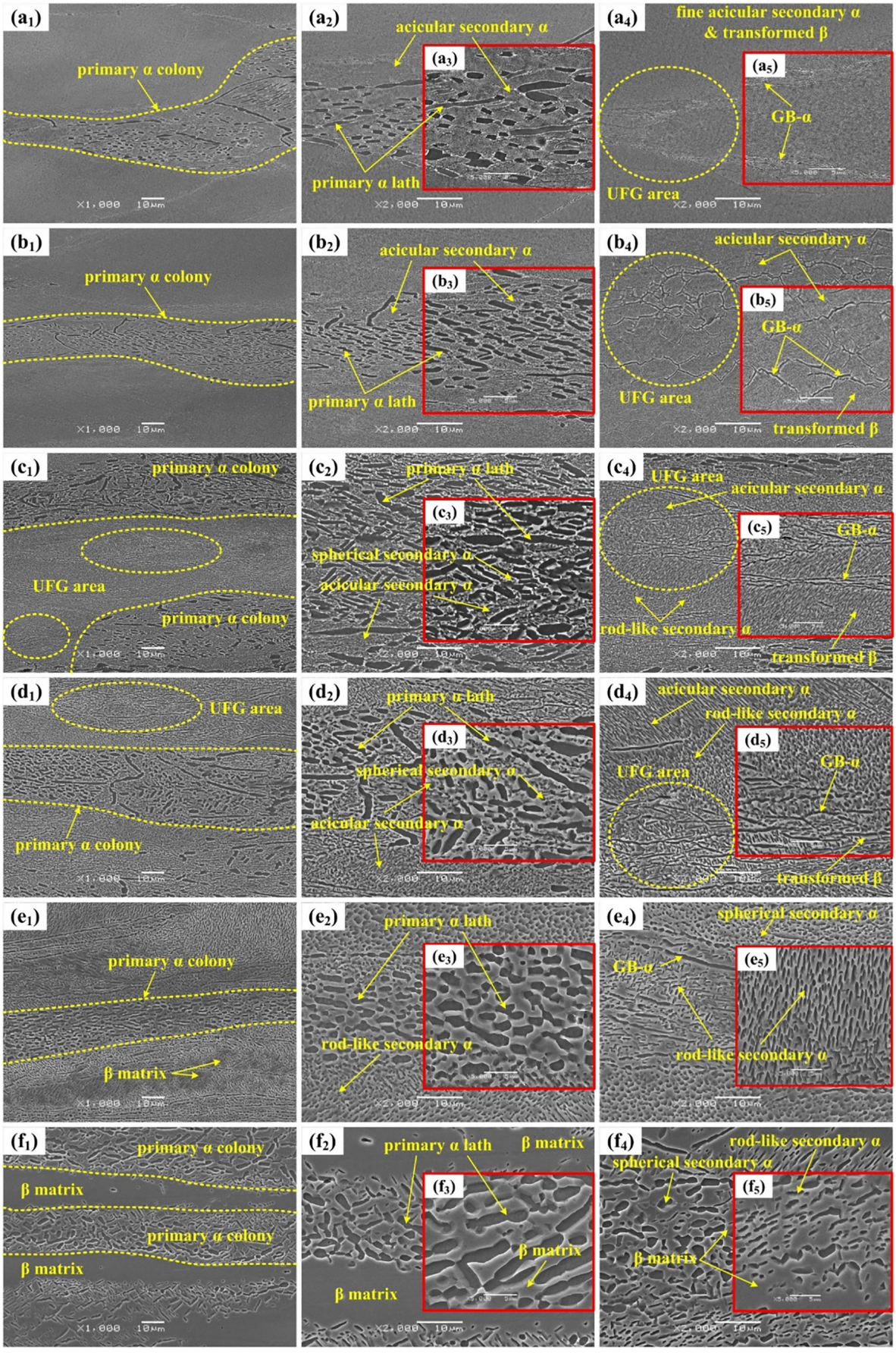

Fig. 14. SEM microstructures of FR-1 alloy heat-treated at: (a_1)-(a_5) 600 °C; (b_1)-(b_5) 650 °C; (c_1)-(c_5) 700 °C; (d_1)-(d_5) 750 °C; (e_1)-(e_5) 800 °C; (f_1)-(f_5) 850 °C, for 1 h, followed by air cooling.

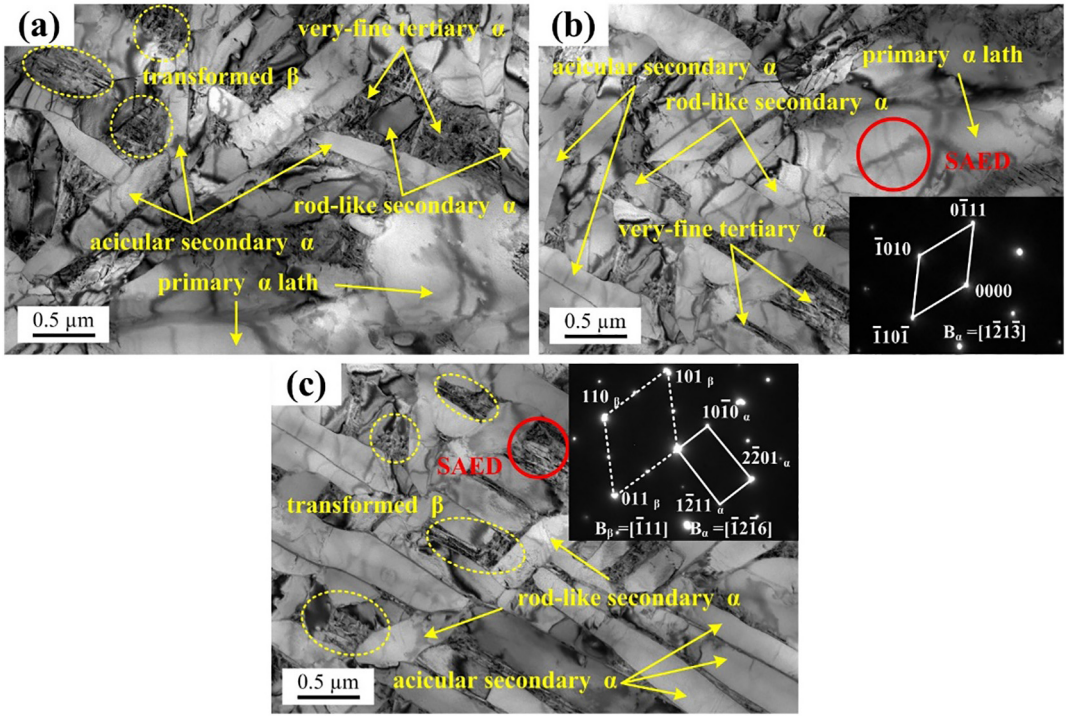

Fig. 15. High magnification AC-TEM images showing the detailed microstructures of FR-1 alloy heat treated at 700 °C for 1 h.

stage, with the UTS lower than 1200 MPa, hardness lower than 400 HV, and ε_f lower than 4.1%.

For FR-4 alloy, as shown in Fig. 18b and Table 3, it is illustrated that its mechanical performance response to heat treatment is similar to that of FR-1 alloy. Both of the strength and hardness of the heat-treated alloy are slightly decreased with increasing the heat treatment temperature from 600 °C to 850 °C, but the respective ductility is firstly increased and then decreased. The highest ductility achieved for the FR-4 alloy is 6.1% when the alloy is treated at 750 °C. Whereas, relatively low ductility and strength/hardness are obtained for FR-4 alloy heat-treated at 800 °C and 850 °C, with the UTS lower than 1030 MPa, hardness lower than 350 HV and ε_f lower than 4.0%. It is also noticeable that FR-1 alloy suggests better strength-ductility matchings than those for FR-4 alloy when they are treated at the same temperature.

Fig. 20 shows the typical SEM fracture surface morphology FR-1 alloys heat-treated at various temperatures. As shown in Fig. 20a, cleavage facets, tear ridges and some small/shallow dimples are observed in the fracture surface of the alloy heat-treated at 600 °C, which indicates that alloy was fractured with the ductile-brittle mixed cleavage mechanism. Similar features are found in the fracture surface of 650 °C-treated FR-1 alloy (see Fig. 20b_1-b_2), showing larger amount and bigger size of dimples than those of the alloy treated at 600 °C, and this result implies the improvement of tensile ductility. A large amount of dispersed and deep dimples appear on the fracture surface of the FR-1 alloy heat-treated at 700 °C and 750 °C, as shown in Fig. 20c_1-c_2 and d_1-d_2, and cleavage fracture characteristics are unobserved. Furthermore, secondary cracks and deep ravines are also observed on the fracture surface of 750 °C heat-treated alloy, suggesting that very high tensile ductility was achieved. For the 800 °C- and 850 °C-heat-treated ones (see Fig. 20e-f), the failure modes of tensile specimens are dominated by complete brittle cleavage mechanism, proved by the large-scale cleavage facets and features of river-like patterns without dispersive dimples on the fracture surface.

4. Discussion

4.1. Microstructural evolution mechanism during TMP

Based on the microstructure observation results of the as-forged alloy pancakes processed following different TMP routes, and with the help of our previous research, the detailed microstructure variation

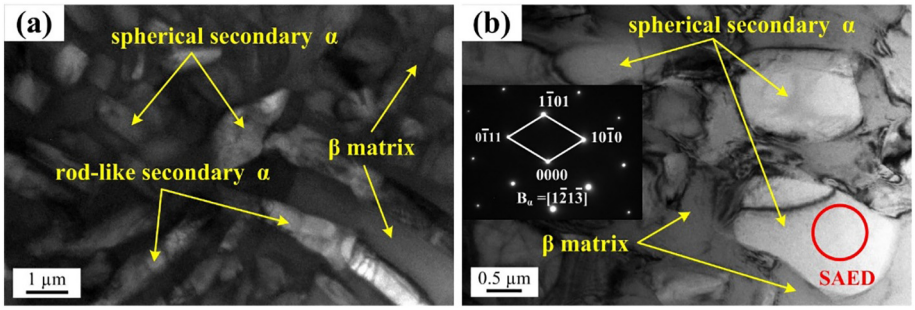

Fig. 16. High magnification TEM images showing the detailed microstructures of FR-1 alloy heat-treated at 850 °C for 1 h.

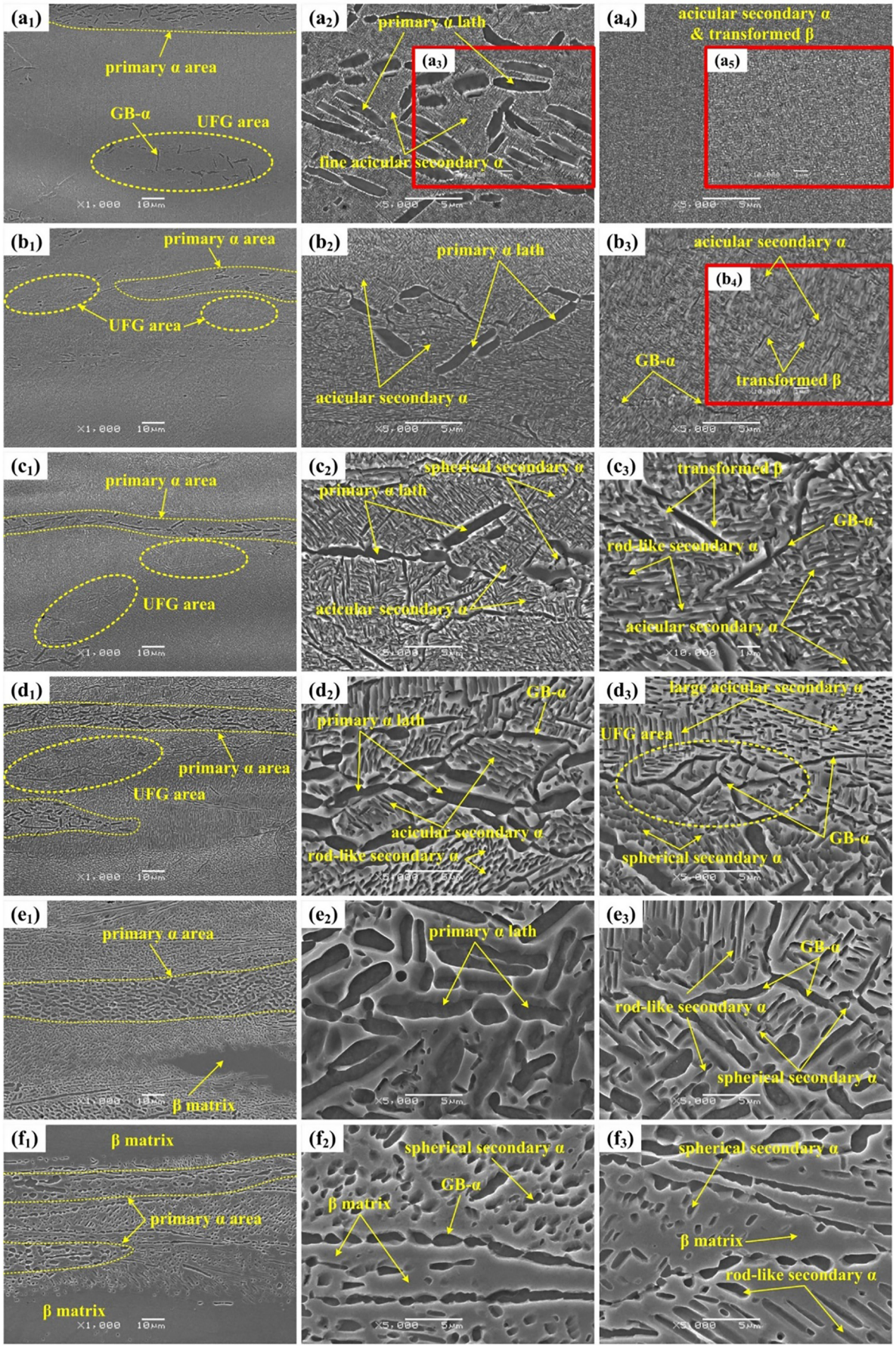

Fig. 17. SEM microstructures of FR-4 alloy heat-treated at: (a_1)-(a_5) 600 °C; (b_1)-(b_4) 650 °C; (c_1)-(c_3) 700 °C; (d_1)-(d_3) 750 °C; (e_1)-(e_3) 800 °C; (f_1)-(f_3) 850 °C, for 1 h, followed by air cooling.

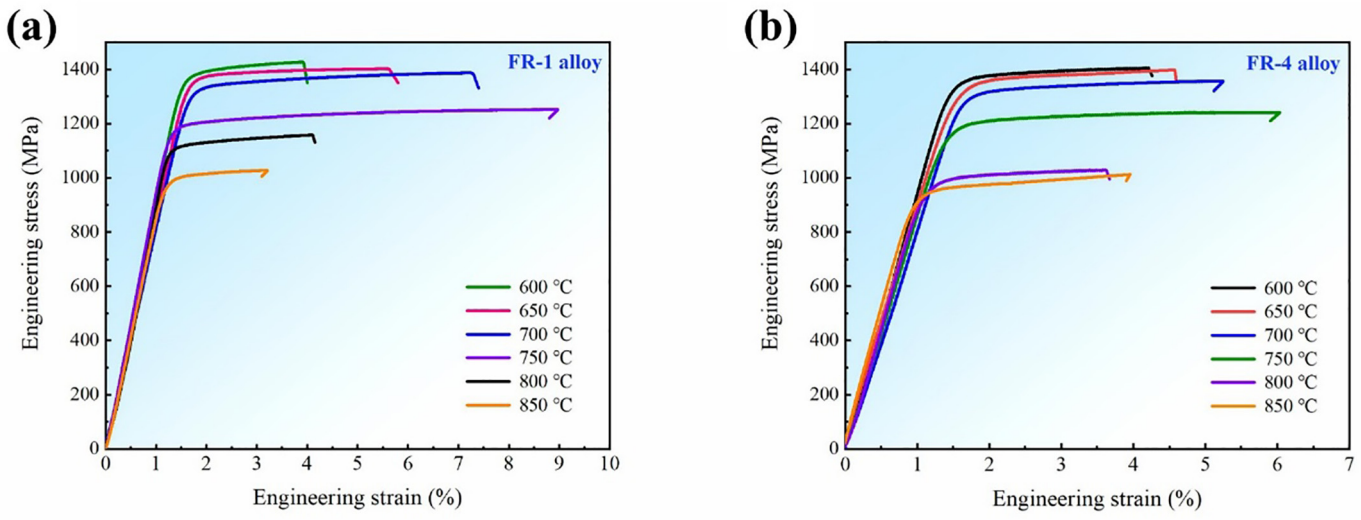

Fig. 18. Typical tensile curves for the heat-treated alloys at various temperatures (600 °C–850 °C): (a) FR-1 alloy; (b) FR-4 alloy.

mechanisms when the PM Ti-5553 alloy is processed via each specific TMP route can be revealed and disclosed.

The microstructural evolution processes of the alloy forged at the potential "best" processing condition (see Fig. 5, 950 °C/~0.01 s^{-1}) can be clarified by the combined microstructure analysis of FR-1 and FR-4 alloys. A schematic diagram is presented in Fig. 21 to demonstrate the detailed microstructure variation processes at this condition. As mentioned in Section 3.1, the original microstructure of as-consolidated alloy is composed of beta phase matrix and a small amount of α/α″ precipitates which are agglomerated, as shown in Fig. 7b, and these features are represented in the sketch of Fig. 21a. While heating the as-consolidated alloy up to 950 °C and held the temperature for 30 mins before forging, the initial α/α″ precipitates would be completely dissolved into β matrix and the β grains are also coarsened slightly due to the heating temperature is close to the measured beta phase transform temperature of 975 °C (as represented in Fig. 21b).

Afterwards, during the hot forging deformation, the microstructure of the alloy is changed significantly to produce the mixed-grain structure consisted of elongated large grains and small equiaxial grains attributed to the concurrent softening mechanisms of localized/partial DDRX and extensive DRV induced by severe plastic deformation (SPD). Furthermore, some α phases are generated dynamically along/near the boundaries of serrated β grains and the newly-formed DDRX grains to form GB-α phase during forging. As is revealed in our preliminary study [28], dynamic α→β phase transformation occurs when the PM Ti-5553 alloy is deformed at 950 °C/0.01 s^{-1}, and the resultant deformed structure after thermal physical simulation is free of α phase. However, the practical forging was not performed/done under isothermal deformation condition as thermal physical simulation, ineluctable die chilling effect would reduce the practical deformation temperature dynamically during forging, although the forging die was preheated up to 500 °C. Furthermore, there is almost no adiabatic temperature rising during hot forging the PM Ti-5553 alloy at 950 °C/0.01 s^{-1}. Because of those two reasons, there is a possibility that a small amount of α phase is formed in the microstructure of FR-1 and FR-4 alloys during forging. Besides, the pre-existed GBs become the preferred nucleation sites for the newly-generated α phase attributed to the local lower nucleation energy and higher elemental diffusion rate. Hereinafter, upon the completion of the forging processes, water quenching process leads to that FR-4 alloy almost keep the currently deformed microstructure composed of elongated β grains with some fine DDRX grains located on the β grain boundary, as represented in Fig. 21c.

During air cooling after hot forging at 950 °C/~0.01 s^{-1} (Fig. 21d), the elongated β grains become wider and coarser with reduction of the grain aspect ratio, forming the microstructure of slightly-elongated CGs in FR-1 alloy. The newly-formed fine DDRX grains also grow coarse with near-equiaxed shape, becoming the UFGs in the microstructure of FR-1 alloy. Meanwhile, large-sized α_p lath colonies are formed by coarsening the unevenly generated GB-α on the prior β-GB. Moreover, GB-α phases that distributed around the newly-formed DDRX grains are developed into the surrounding α phases of the UFGs, while very fine α precipitations are also precipitated at the same time in some β-matrix areas to form β_{TF} structure.

For the FR-2 alloy (the corresponding schematic diagram is presented in Fig. 22), the initial microstructure and microstructure changes are similar with that of FR-1 alloy before forging, as shown in Fig. 22a and b. The different microstructural evolution characteristics occur in the process of hot forging due to different deformation strain rates

Table 2
Mechanical properties of FR-1 alloy after heat treatment at various temperatures.

Heat treatment temperature	Yield stress[a] (YS/MPa)	Ultimate tensile stress (UTS/MPa)	Strain at failure (ε_f/%)	Microhardness (MH/HV)
600 °C	1335.5	1420.2	4.0	488.6
650 °C	1304.6	1392.8	5.6	461.2
700 °C	1295.3	1386.5	7.3	453.2
750 °C	1170.5	1252.3	9.0	410.2
800 °C	1075.9	1157.2	4.1	388.8
850 °C	988.5	1030.0	3.3	359.4

[a] Yield point is set at 0.2% plastic strain.

Table 3
Mechanical properties of FR-4 alloy after heat treatment at various temperatures.

Heat treatment temperature	Yield stress[a] (YS/MPa)	Ultimate tensile stress (UTS/MPa)	Strain at failure (ε_f/%)	Microhardness (MH/HV)
600 °C	1320.6	1405.5	4.2	468.9
650 °C	1299.5	1383.2	4.6	455.2
700 °C	1258.6	1357.5	5.2	428.8
750 °C	1158.5	1235.7	6.1	397.6
800 °C	965.5	1025.2	3.6	347.9
850 °C	957.9	1013.5	4.0	334.5

[a] Yield point is set at 0.2% plastic strain.

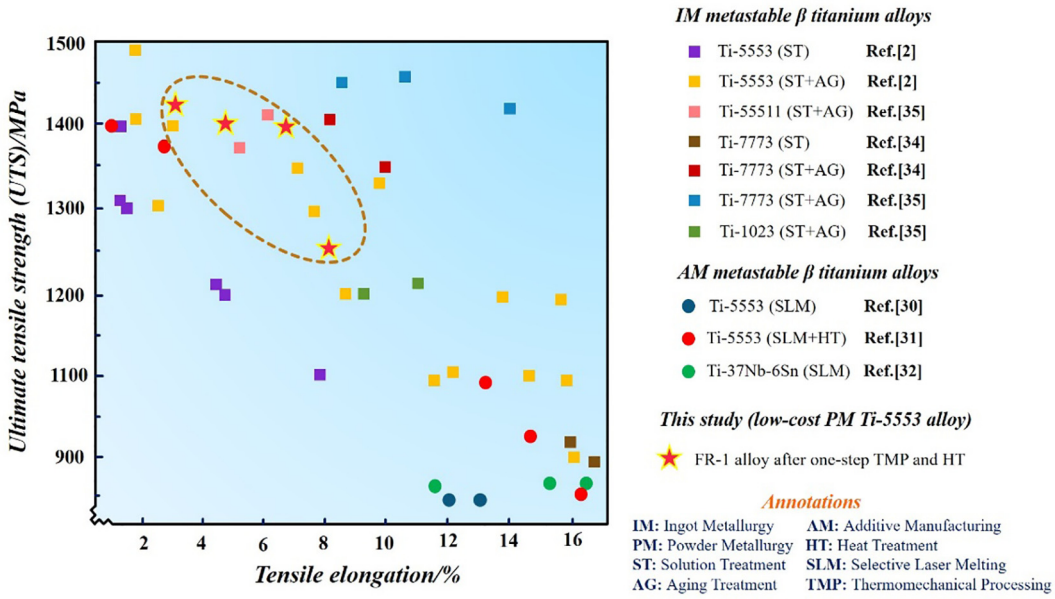

Fig. 19. Comparison of tensile properties between the low-cost PM Ti-5553 alloy (in this study, heat-treated FR-1 alloy) and some representative metastable β titanium alloys fabricated by IM and other PM (AM) approaches [2,30–35].

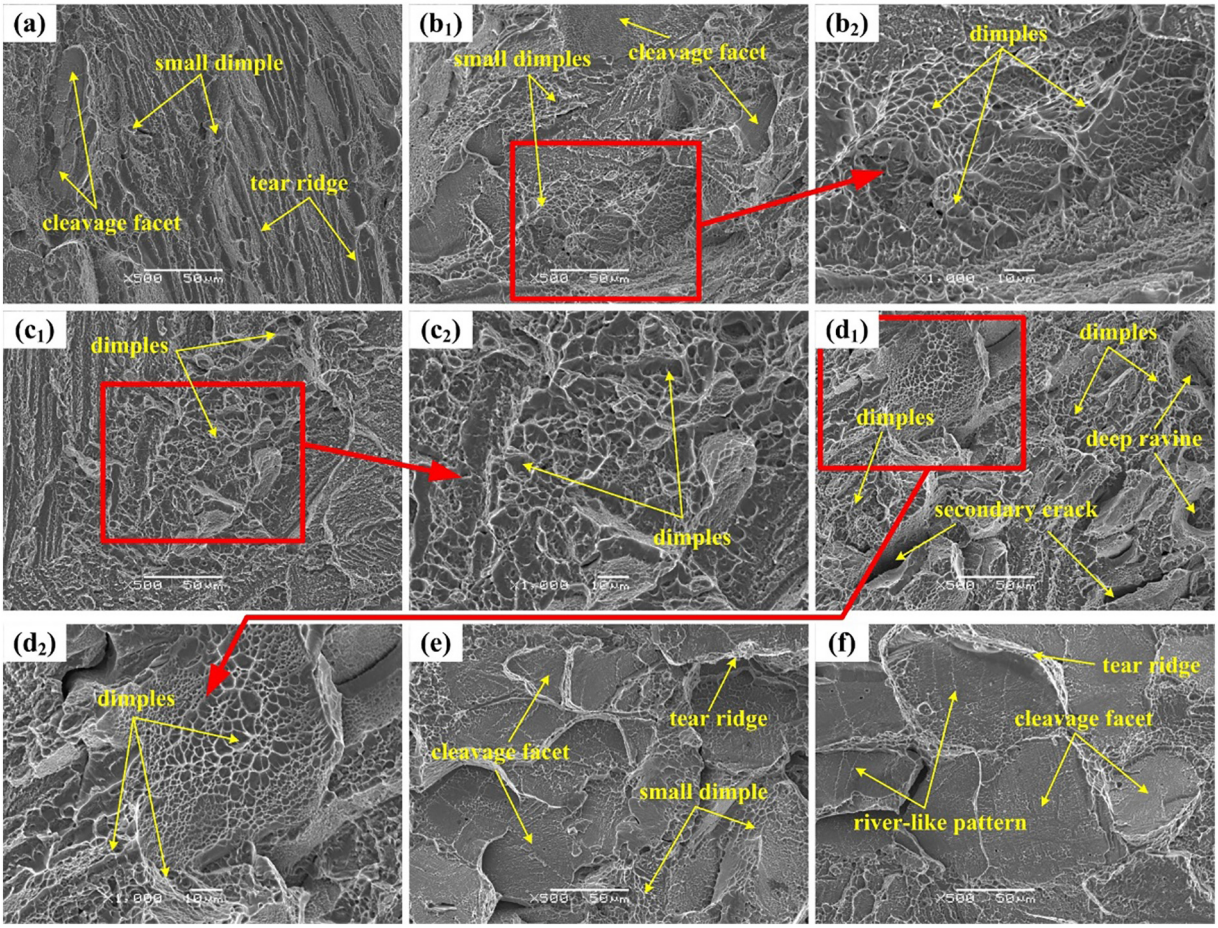

Fig. 20. Representative SEM fracture surface of the heat-treated FR-1 alloy after tensile testing: (a) 600 °C; (b_1)-(b_2) 650 °C; (c_1)-(c_2) 700 °C; (d_1)-(d_2) 750 °C; (e) 800 °C; (f) 850 °C.

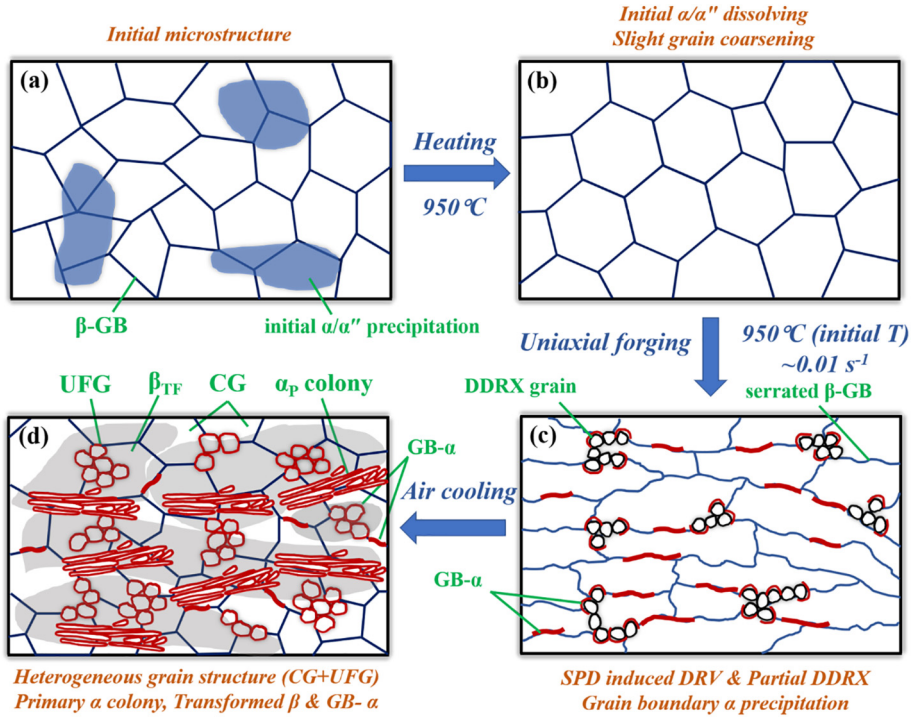

Fig. 21. Schematic illustration of the microstructural evolution mechanism for FR-4 and FR-1 alloys during TMP: (a) initial microstructure; (b) microstructure after heating; (c) microstructure evolution during forging for FR-4 alloy (after WQ); (d) final microstructure after AC for FR-1 alloy.

employed. It is also suggested that the high-strain-rate deformation impedes the occurrence of DDRX in PM alloy but triggers strong DRV comparing to low-strain-rate deformation at the temperature of 950 °C. Thus, the PM Ti-5553 alloy would show strong DRV characteristics in the hot forging at 950 °C/~0.5 s^{-1}, (Fig. 22c). Moreover, there is no GB-α generated dynamically during forging at this condition because of α phase is difficult to nucleate with the lacking of effective thermal activation and elemental diffusion in relatively short forging time (FR-2 alloy has only 2% of the deformation time for FR-1/FR-4 alloys) [36,37]. The high-strain-rate deformation and strong DRV also lead to

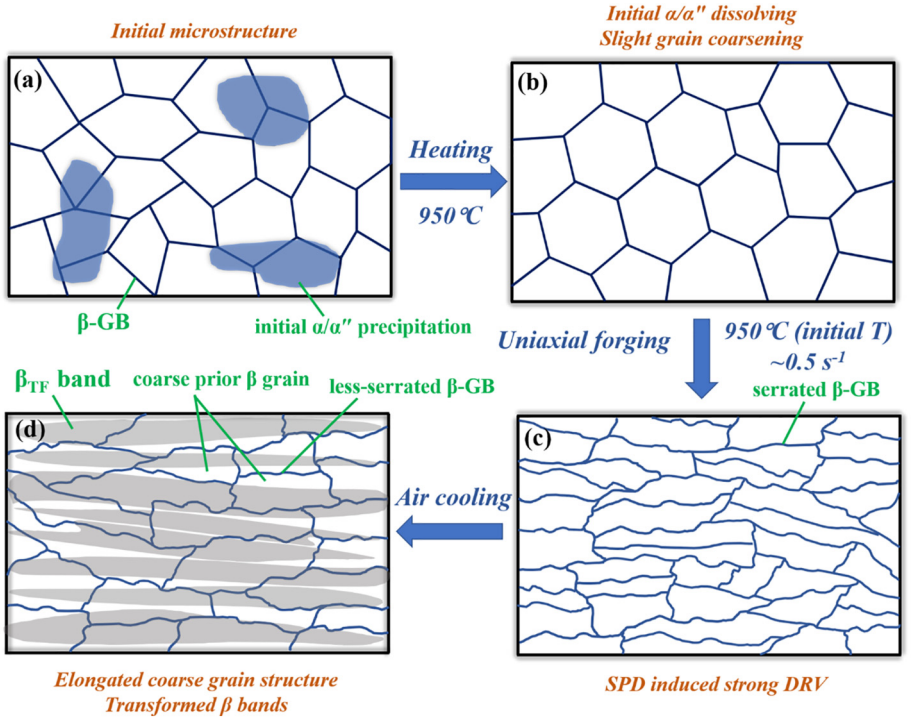

Fig. 22. Schematic illustration of the microstructural evolution mechanism for FR-2 alloy during TMP: (a) initial microstructure; (b) microstructure after heating; (c) microstructure evolution during forging; (d) final microstructure after AC.

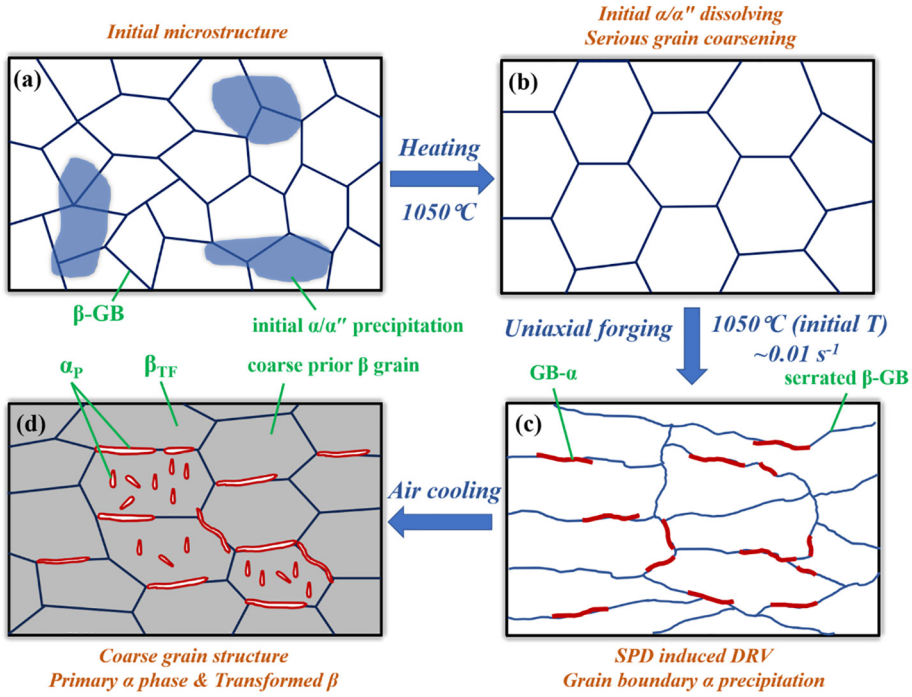

Fig. 23. Schematic illustration of the microstructural evolution mechanism for FR-3 alloy during TMP: (a) initial microstructure; (b) microstructure after heating; (c) microstructure evolution during forging; (d) final microstructure after AC.

the formation of the narrow elongated-grain structure with serrated GB. These characteristics are considered to have decisive effects for forming the final microstructure for FR-2 alloy after air cooling from the hot forging temperature, as indicated in Fig. 22d. After the alloy is air-cooled to room temperature, the coarse prior β grains still remain elongated shape with serrated GB due to inadequate thermal diffusion. The fast forging also introduces higher storage energy and dislocation density in the alloy, resulting in the precipitation of larger-sized acicular α in widespread β_{TF} bands after air cooling [38–40].

Schematic diagram of Fig. 23 shows the microstructural evolution of FR-3 alloy during hot forging at 1050 °C/~0.01 s^{-1} and subsequent air-cooling processes. Comparing to the alloys processed in (α + β) region, the grain structure of FR-3 alloy is seriously coarsened when it is heated up to 1050 °C (75 °C above the β transformation temperature), as illustrated in Fig. 23b [41–43]. Considering the microstructure features of FR-3 alloy and the preliminary results, it is suggested that DRV is the predominated behaviour rather than DRX for the PM Ti-5553 alloy processed at this high temperature (1050 °C). Similar to FR-1 and FR-4 alloys, dynamic initiation of GB-α phase is induced by the low-strain-rate deformation and the dynamic reduction of the actual forging temperature (Fig. 23c). Subsequently, wide and elongated grains are evolved into coarse grains with near-equiaxed shape during air cooling (Fig. 23d). Meanwhile, large α_p phases, which are distributed along β-GB and in the inside of the coarse grains, are growing coarse. The proportion of α_p phase in FR-3 alloy is lower than that of FR-1 alloy, this is because the GB density is low and there are no DDRX grains in FR-3 alloy. Additionally, very fine α precipitates are also formed in the β matrix to become β_{TF} structure. The amount of β_{TF} structure in the FR-3 alloy is larger than that in FR-1 alloy, attributed to higher initial forging temperature and subsequent longer cooling time.

4.2. Microstructural evolution mechanism during heat treatment

From above microstructure observation results of the heat-treated alloys, it is suggested that the processed PM Ti-5553 alloys have serious microstructure heredity (from the microstructure of the TMPed alloys) and high microstructural sensitivity to the variable (heat treatment temperature) during post-HT. In this section, the specific and detailed microstructural evolution mechanisms of the as-forged alloys (FR-1 and FR-4), during post-HT, are discussed.

Fig. 24 shows the schematic diagram illustrating the microstructure evolution mechanisms of FR-1 alloy during heat treatment. When the alloy is treated at the temperatures of 600 °C to 750 °C (see Fig. 24a and b), dispersed acicular α_s phases (some rod-like and spherical α_s phases are also visible in the 700 °C and 750 °C heat-treated samples) are able to be generated in the β matrix and previous β_{TF} structure due to the effects of thermal activation and elemental diffusion. Meanwhile, the previous β_{TF} structure is inclined to expand and form a certain amount of nano-sized α_t precipitates internally at these heat-treated temperatures, and then become new β_{TF} structure that dominates the FR-1 alloy (the previous precipitation-free regions are eliminated). The CG/UFG grain mixture and lath α_p colonies appeared in the heat-treated FR-1 alloy are integrally inherited from the original as-forged microstructure. Hence, the heat-treated FR-1 alloy exhibits a heterogeneous grain microstructure that includes tri-hierarchical α precipitations.

The tri-modal precipitation structure has also been obtained in some other IM titanium alloys such as TA-15 (near-α type, Ti-6Al-2Zr-1Mo-1V) [44–47], TC-11 (α + β type, Ti-6.5Al-3.5Mo-1.5Zr-0.3Si) [48] and modified Ti-6Al-4V [49] alloys, which has been verified to have a great contribution to their excellent mechanical properties. However, the tri-modal structures in those IM alloys are introduced through the combination of multiple-step TMP and complicated post-HT processes. The formation of tri-modal α precipitation structure in the studied PM Ti-5553 alloy (via one-step forging plus simple post-heat treatment) is attributed to the PM alloy we produced has fine-grain structure and high oxygen content. Furthermore, the morphology of α_p phase is different between the studied PM and other IM Ti-5553 alloys. The α_p phases in the IM titanium alloys with tri/bi-modal α precipitation structure usually have the equiaxed shape and are generally distributed uniformly

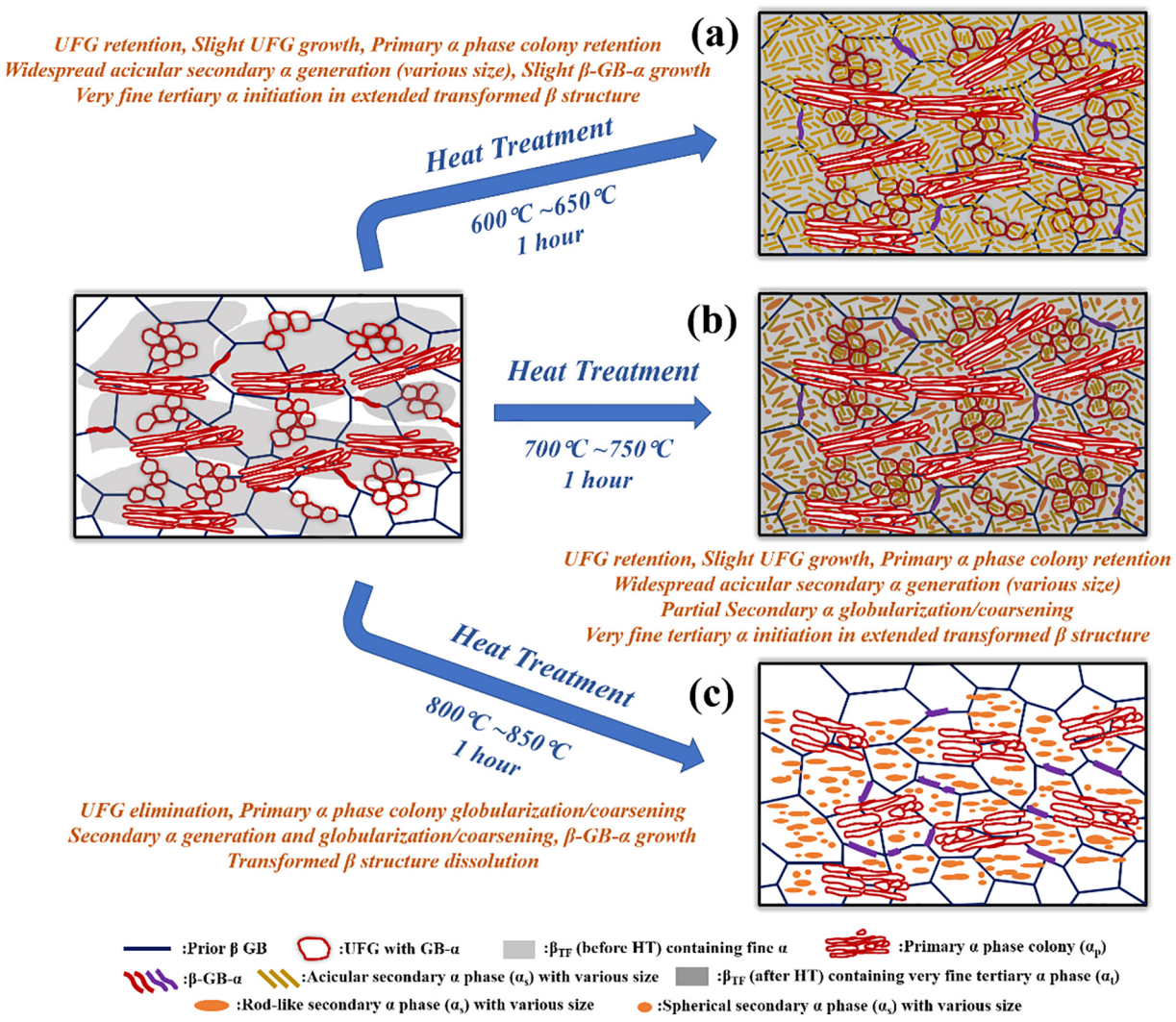

Fig. 24. Schematic demonstration of the microstructural evolution mechanism for FR-1 alloy during heat treatment at various temperatures: (a) 600 °C–650 °C; (b) 700 °C–750 °C; (c) 800 °C–850 °C.

in the microstructure, while the α_p phases in the PM Ti-5553 alloy possess a lathed shape and the α_p laths are gathered to form α_p colonies. These characteristics are related to the single uniaxial open-die forging process.

The morphology of α_s phase is sensitive to the heat treatment temperature. The size of acicular α_s phase is getting larger as increasing the heat treatment temperature from 600 °C to 750 °C, leading to the formation of the rod-like and spherical α_s phases. Meanwhile, UFG in the microstructure also is coarsened after heat treatment, and its growth becomes more obvious at relatively high heat treatment temperatures. However, α_p colonies and GB-α show relatively high thermal stabilities at the temperature range of 600 °C to 750 °C, and their structures are almost kept unchanged.

When the FR-1 alloy is heat-treated at the temperatures of 800 °C to 850 °C (see Fig. 24c), the alloy's microstructure is significantly changed comparing to the alloy treated at lower temperatures. The tri-modal α precipitation structure and grain gradient are disappeared as the dissolution of β_{TF} structure and UFG's growth happen at the temperatures higher than 800 °C. These results indicate that the critical heat treatment temperature for FR-1 alloy to maintain the harmonious coexistence of grain heterogeneity and α precipitation hierarchy is 750 °C, and the coarsening and spheroidization processes of α_s phase, α_p colonies and GB-α phase also are accelerated with increasing the heat treatment temperature, to form the rod-like and spherical α_s phases with remarkable reduction of their phase aspect ratios.

Actually, the coarsening and spheroidization phenomena of α_s phase, α_p colonies and GB-α phase are processed with the mechanism of static α phase globularization. The static globularization is only driven by thermal activation energy without external stress during post-HT. According to the series of researches carried out by Xu et al. [50–52] on TC-17 alloy (α + β type, Ti-5Al-2Sn-2Zr-4Mo-4Cr), the static α phase globularization processes during HT can be divided into two stages. The first stage is the generation of detached β phase due to release of distortion energy (after TMP) and thermal-induced elemental diffusion. Subsequently, the α stabilizers diffuse from the terminal position to the low-curvature position controlled by termination migration and Ostwald ripening mechanisms, resulting in α phase's globularization and coarsening during post-HT. These explain why larger globularization and coarsening degrees are observed for FR-1 alloy at the heat treatment temperature of > 800 °C (no phase globularization happens at 600 °C–650 °C, partial α_s phase globularization is observed at 700 °C–750 °C, while remarkable globularization/coarsening processes of α_s phase, α_p colonies and GB-α appear at 800 °C–850 °C). This is because higher thermal driving

force is provided for elemental diffusion at higher temperatures than that at lower heat treatment temperatures, thus promoting the α precipitation's static globularization and coarsening. Furthermore, α_s phases are observed to suffer a higher degree of globularization/coarsening than α_p and GB-α phases at the same heat treatment temperature, this is because α_s phase has smaller size and relatively less elemental stability, which helps enhance the termination migration process and Ostwald ripening effects.

Fig. 25 exhibits the schematic diagram demonstrating the microstructure evolution mechanisms for FR-4 alloy during heat treatments. Similar to the FR-1 alloy, FR-4 alloy also possesses the heterogeneous grain structure with tri-hierarchical α precipitations after heat treatment at 600 °C–750 °C (Fig. 25 a and b). However, the width and amount of α_p colony are narrower and smaller in the treated FR-4 alloy than those in the treated FR-1 alloy, because α_p is newly formed from GB-α in FR-4 alloy but is inherited from the as-forged stage for FR-1 alloy. Different from the air-cooled FR-1 alloy after TMP, the deformation energy induced by significant plastic deformation during TMP has remained in the water-quenched FR-4 alloy. Therefore, post-HT becomes the great chance for the plentiful deformation storage energy in FR-4 alloy to be released intensively, which leads to the belated formation of large-scale lath α_p colony. The higher amount of released storage energy for FR-4 alloy during post-HT also makes it understandable that why the size and static globularization tendency of α_s phases are bigger and stronger for FR-4 alloy than those for FR-1 alloy at the same post-HT temperature between 600 °C–750 °C.

After heat-treating at relatively high temperatures of 800 °C and 850 °C, similar microstructures are observed for FR-1 and FR-4 alloys (see Fig. 14e_1-f_3 and Fig. 17e_1-f_3), suggesting that the primary microstructures of FR-4 and FR-1 are evolved similarly during post-HT at these conditions (as illustrated in Fig. 25c), except the size and width of globularized α_p colony is smaller and narrower in FR-4 alloy than those in FR-1 alloy.

4.3. The origin of excellent strength-ductility combination

It has been illustrated that excellent strength-ductility matchings are successfully achieved in our newly-designed cost-affordable PM Ti-5553 alloy (FR-1 alloy heat-treated at 700 °C and 750 °C). The origin is expected to come from the harmonious synergy containing distinctive chemical composition, heterogeneous grain structure and hierarchical precipitation features:

(1) High interstitial element (O and N) contents for strength. The studied PM alloy has obvious higher oxygen (0.36 wt%) and nitrogen content (0.021 wt%) than those of IM alloys, which can be beneficial to the high strength of the alloy. These interstitial elements are able to strengthen α solid solution with multi-

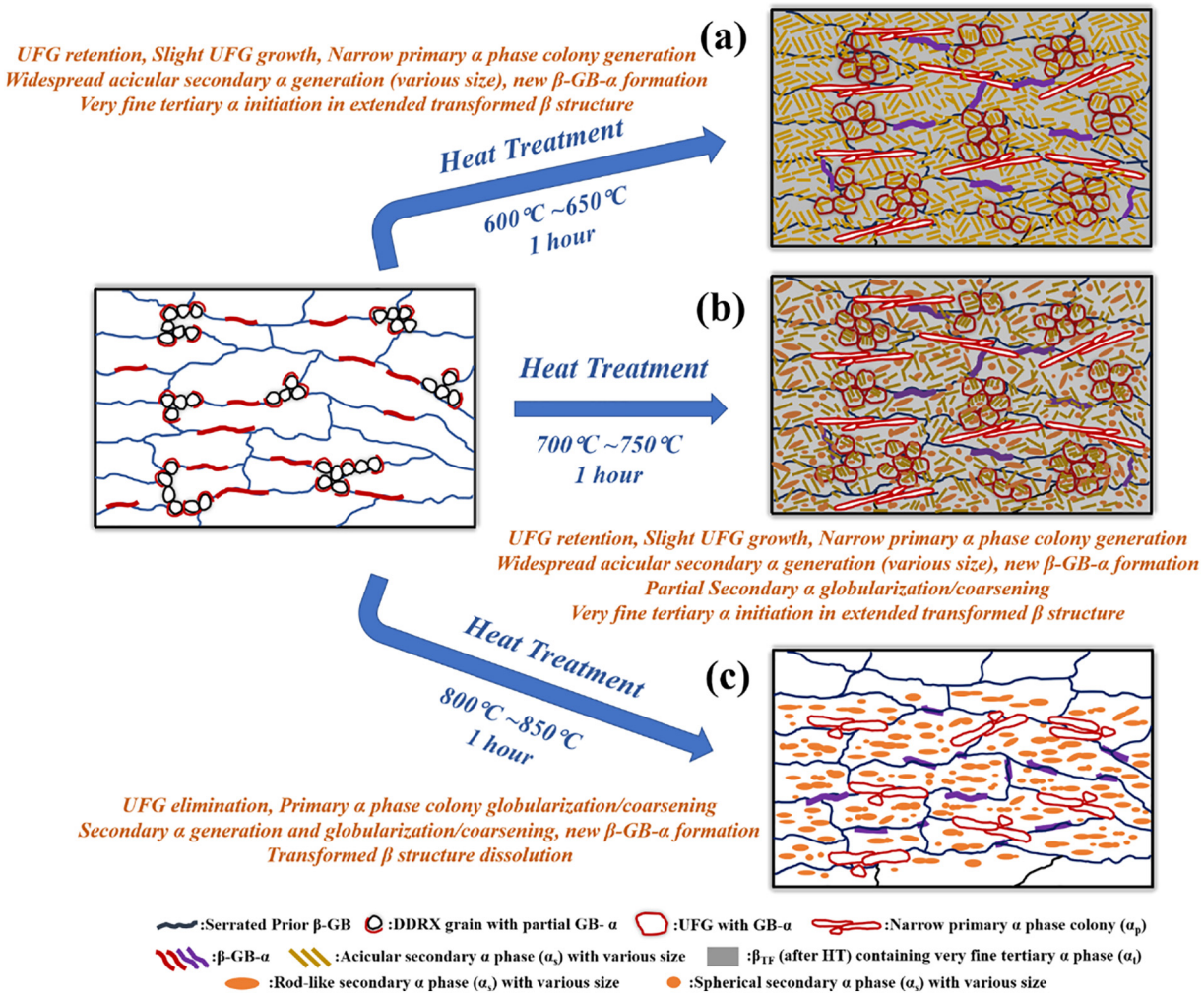

Fig. 25. Schematic demonstration of the microstructural evolution mechanism for FR-4 alloy during heat treatment at various temperatures: (a) 600 °C–650 °C; (b) 700 °C–750 °C; (c) 800 °C–850 °C.

hierarchy by occupying the octahedral interstices in the crystal lattice of Ti [53,54] and pinning dislocations movement remarkably during deformation in the O (N)-rich PM alloy [55].

(2) Heterogeneous grain structure composed of CG and UFG for strength and ductility. The UFG can act as the reinforcement and significantly increase the alloy's strength by blocking dislocation movement and grain sliding, while the CG can act as a dislocation sink and absorb higher energy to accommodate deformation for achieving good ductility [56–58]. This kind of heterogeneous grain structure obtained in FR-1 alloy has also been introduced in many advanced metallic materials [59–62] including metastable β titanium alloy [63] and β titanium alloy [64] to achieve the ultra-high-strength without a significant trade-off in ductility [56,65,66].

(3) Complex α phase hierarchy composed of large-sized α_p colony, high-density rod-like/spherical α_s, nanoscale-dispersed α_t and some GB-α for strength and ductility. When it is subjected to high strength, the α_s and α_t phases initiated by diffusion-induced transformation can introduce severe lattice distortion in their structure, and this limits the mobility of the dislocations during tensile deformation by the highly-defected substructures. Moreover, the high-density distributions of α_s and α_t phases introduce a large amount of α/β interface in the alloy, causing significant interface strengthening effect. Thirdly, α_s and α_t phases in FR-1 alloy also have the configuration of multi-variant (dimension and direction) precipitation (see Fig. 15), which further increase the strength by extra dislocation slip transfer resistance. The widespread multi-hierarchical α structure is also an important factor to be considered for the moderated ductility. After heat treatment, the large-sized α_p phase is relatively soft in the microstructure of metastable β titanium alloys [22,67], comparing to α_s phase and β_{TF} structure. During tensile deformation, large lath α_p colony in the alloy can accommodate dislocation movement, sustain the displacement, and absorb the external deformation energy, thus increasing the alloy's ductility to some extend [68,69]. Furthermore, the dispersed α phases with multi-hierarchy in the microstructure can improve the stress/strain compatibility, homogenize the strain partitioning and resist the cracking propagation during deformation, and thus help to enhance the ductility of the alloy as well.

4.4. Mechanical property variation mechanism

From the mechanical property examination results, it is clearly demonstrated that the properties of the manufactured PM Ti-5553 alloy are determined by the microstructural characteristics introduced by varying processing and heat treatment processes.

There are obvious differences between the mechanical properties of the as-forged PM Ti-5553 alloys processed by different forging routes, attributed to the discrepancies in the resultant microstructures. FR-1 alloy exhibits the highest strength, hardness and ductility among the as-forged alloys, followed by FR-2 alloy, FR-3 alloy, and then FR-4 alloy. The incorporation of positive grain structure heterogeneity and precipitation hierarchy is observed in FR-1 alloy, while the microstructure of FR-2 alloy is composed of elongated β grains and dispersed β_{TF} band. FR-3 alloy shows seriously coarsened β grains with widespread β_{TF} structure in its microstructure, while there are only β grains and very limited-amount GB-α in the water-quenched FR-4 alloy. These results confirm that the grain structure and the precipitation distribution play important roles in mechanical performance of PM Ti-5553 alloy. The presences of α_p and fine grains in the microstructure are beneficial to the outstanding mechanical properties. On the contrary, simply coarsened grains and insufficient/single precipitation in the microstructure are verified against the improvement of mechanical performances. Meanwhile, it is also revealed that the previously-predicated potential "best" TMP condition produces the alloy with the highest mechanical properties at as-forged stage. Conversely, TMP conducted in single β region and/or with high strain rate has no effects on improving the mechanical properties of this studied PM alloy.

In terms of the effect of heat treatment temperature (take FR-1 alloy as the example), the existence of fine and large number of α_s/α_t phases generates high α/β interface density and a large number of substructures, and these would cause a significant strengthening effect on the alloy. However, the over-strong strengthening effect also leads to the degradation of ductility (at 600 °C and 650 °C). That is why the ductility of heat-treated alloy is increased dramatically with increasing the heat treatment temperature from 600 °C to 750 °C, and the superior strength-ductility balances are achieved for the 700 °C and 750 °C heat-treated alloy. When the α_p and α_s phases are completely globularized/coarsened for the alloy treated at 800 °C–850 °C, both strength and ductility are significantly decreased for the alloy. Furthermore, a significant reduction in the amount of α precipitation and subsequently reduced α/β interface, as well as the lack of UFG and tri-hierarchical α structure in the microstructure are other reasons to cause low strength and low ductility for 800 °C and 850 °C heat-treated alloy comparing to the lower-temperature-treated alloy. Because of the completely globularized/coarsened α_p/α_s phases and the absence of α_t phases (in β_{TF} structure) in the microstructure after post-HT at 800 °C and 850 °C, both the α precipitation phase density and α/β interface density are reduced remarkably, which makes the alloy less strengthened. UFGs no longer exist in the microstructure at these two conditions, and this makes the strength reduction situation even more serious. Moreover, the loss of tri-hierarchical α structure and emergence of precipitation-free regions also make the alloy brittle. Additionally, relatively inhomogeneous precipitation distribution and single β matrix in the microstructure lead to degradation of stress/strain compatibility and easy propagation of cracking during tensile deformation. Therefore, FR-1 alloy has low strength and poor ductility at 800 °C, and this situation becomes even worse at 850 °C.

For FR-1 alloy and FR-4 alloy after heat treatment, the microstructural differences between these two alloys become the width of α_p colony and the static globularization degree of α_s phases. The width of α_p colonies is narrower in the heat-treated FR-4 alloy (about 10 μm) than that in the heat-treated FR-1 alloy (larger than 30 μm), while the static globularization tendencies of α_s phases are significantly stronger for FR-4 alloy than those for FR-1 alloy at the same post-HT temperatures (see Figs. 23 and 24). Thus, combining with their mechanical properties, it can be concluded that wide/massive α_p colony and appropriately-globularized α_s phases in the microstructure are beneficial to achieve the balanced mechanical properties for the PM Ti-5553 alloy.

5. Conclusions

In this work, a cost-affordable and qualified metastable β titanium alloy has been manufactured from powder mixture by the designed thermomechanical consolidation and processing approach in a short time. The microstructures and mechanical properties of the alloy at varying conditions were characterized and examined to reveal the microstructural evolution mechanism and to disclose the microstructure-property relationship for the alloy. Primary conclusions are summarized as follows:

(1) Homogeneous macrostructure and fine-grain microstructure without undissolved particles and big pores are obtained for the alloy after thermomechanical powder consolidation thanks to the concurrent effect of external deformation and high-temperature diffusion.
(2) Single-step open-die forging based on route designing is verified

to produce full-dense PM alloy pancake with high strength.

(3) Superior strength-ductility combinations are achieved for FR-1 alloy after heat treatment at 700 °C and 750 °C for only one hour, with tensile UTS of 1386.5 MPa and ε_f of 7.3% for the 700 °C-treated alloy, and UTS of 1252.3 MPa and ε_f of 9.0% for the 750 °C-treated alloy. These excellent mechanical properties are comparable or even better than those of some PM-manufactured and IM-manufactured metastable β titanium alloys with relatively high cost and time consumption.

(4) The excellent strength-ductility synergy for the alloy is realized by incorporating multiple-hierarchy precipitation into heterogeneous grain structure. Conversely, the absences of primary α phase and grain size heterogeneity in the alloy's microstructure lead to the deterioration of resultant strength and ductility.

Nevertheless, the limitation of this study also deserves further discussion. The developed TPC approach was employed to consolidate the PM alloy billet with a diameter of 58 mm in this work, this size is enough for laboratory-engineering processing investigation, but gaps are definitely remained for actual industrial-scaled processing. Moreover, considering practical engineering applications, fracture toughness and fatigue resistance are expected to be further examined for the PM Ti-5553 alloy to provide systematic mechanical performance evaluation, and they (component size magnification and further performance evaluation) have now become ongoing investigations. Besides, simple forging and heat treatments were designed in the current work to minimize the cost of processing high-quality PM Ti-5553 alloy component. It is also valuable to design more complicated TMP and post-heat treatment processes for the PM Ti-5553 alloy to achieve even higher mechanical properties.

Data availability

All data included in this study can be shared directly with the interested researchers from the corresponding author on request.

Declaration of Competing Interest

The authors declare that they have no known competing financial interests or personal relationships that could have appeared to influence the work reported in this paper.

Acknowledgements

The financial supports from New Zealand Ministry of Business, Innovation and Employment (UOWX1402) and Science and Technology Major Project of Shaanxi Province (2020-zdzx04-01-02) are gratefully acknowledged.

References

[1] J.D. Cotton, R.D. Briggs, R.R. Boyer, S. Tamirisakandala, P. Russo, N. Shchetnikov, J.C. Fanning, State of the art in beta titanium alloys for airframe applications, JOM 67 (2015) 1281–1303.

[2] S. Shekhar, R. Sarkar, S.K. Kar, A. Bhattacharjee, Effect of solution treatment and aging on microstructure and tensile properties of high strength β titanium alloy, Ti-5Al-5V-5Mo-3Cr, Mater. Des. 66 (2015) 596–610.

[3] P. Barriobero-Vila, G. Requena, S. Schwarz, F. Warchomicka, T. Buslaps, Influence of phase transformation kinetics on the formation of α in a β-quenched Ti-5Al-5Mo-5V-3Cr-1Zr alloy, Acta Mater. 95 (2015) 90–101.

[4] Z.Z. Fang, J.D. Paramore, P. Sun, K.S.R. Chandran, Y. Zhang, Y. Xia, F. Cao, M. Koopman, M. Free, Powder metallurgy of titanium-past, present, and future, Int. Mater. Rev. 63 (2017) 407–459.

[5] C.X. Cui, B.M. Hu, L.C. Zhao, S.J. Liu, Titanium alloy production technology, market prospects and industry development, Mater. Des. 32 (2011) 1684–1691.

[6] A. Devaraj, V.V. Joshi, A. Srivastava, S. Manandhar, V. Moxson, V.A. Duz, C. Lavender, A low-cost hierarchical nanostructured beta-titanium alloy with high strength, Nat. Commun. 7 (2016) 11176.

[7] S.H. Hong, Y.J. Hwang, S.W. Park, C.H. Park, J.T. Yeom, J.M. Park, K.B. Kim, Low-cost beta titanium cast alloys with good tensile properties developed with addition of commercial material, J. Alloys Compd. 793 (2019) 271–276.

[8] F.H. Froes, M.N. Gungor, M.A. Imam, Cost-affordable titanium: the component fabrication perspective, JOM 59 (2007) 28–31.

[9] M. Ashraf Imam, F.H.S. Froes, Low cost titanium and developing applications, JOM 62 (2010) 17–20.

[10] F.H. Froes, D. Eylon, Powder-metallurgy of titanium-alloys, Int. Mater. Rev. 35 (1990) 162–182.

[11] G.A. Wen, P. Cao, B. Gabbitas, D. Zhang, N. Edmonds, Development and design of binder systems for titanium metal injection molding: an overview, Metall. Mater. Trans. A 44A (2013) 1530–1547.

[12] D.D. Gu, W. Meiners, K. Wissenbach, R. Poprawe, Laser additive manufacturing of metallic components: materials, processes and mechanisms, Int. Mater. Rev. 57 (2012) 133–164.

[13] M. Qian, Y.F. Yang, M. Yan, S.D. Luo, Design of low cost high performance powder metallurgy titanium alloys: some basic considerations, Key Eng. Mater. 520 (2012) 24–29.

[14] D.G. Savvakin, A. Carman, O.M. Ivasishin, M.V. Matviychuk, A.A. Gazder, E.V. Pereloma, Effect of iron content on sintering behavior of Ti-V-Fe-Al near-β titanium alloy, Metall. Mater. Trans. A 43 (2011) 716–723.

[15] A. Carman, L.C. Zhang, O.M. Ivasishin, D.G. Savvakin, M.V. Matviychuk, E.V. Pereloma, Role of alloying elements in microstructure evolution and alloying elements behaviour during sintering of a near-β titanium alloy, Mater. Sci. Eng. A 528 (2011) 1686–1693.

[16] Y.F. Yang, S.D. Luo, G.B. Schaffer, M. Qian, Sintering of Ti-10V-2Fe-3Al and mechanical properties, Mater. Sci. Eng. A 528 (2011) 6719–6726.

[17] S.D. Luo, Y.F. Yang, G.B. Schaffer, M. Qian, Warm die compaction and sintering of titanium and titanium alloy powders, J. Mater. Process. Technol. 214 (2014) 660–666.

[18] M. Ahmed, D. Wexler, G. Casillas, D.G. Savvakin, E.V. Pereloma, Strain rate dependence of deformation-induced transformation and twinning in a metastable titanium alloy, Acta Mater. 104 (2016) 190–200.

[19] M. Ahmed, D. Wexler, G. Casillas, O.M. Ivasishin, E.V. Pereloma, The influence of β phase stability on deformation mode and compressive mechanical properties of Ti-10V-3Fe-3Al alloy, Acta Mater. 84 (2015) 124–135.

[20] M. Ahmed, D.G. Savvakin, O.M. Ivasishin, E.V. Pereloma, The effect of cooling rates on the microstructure and mechanical properties of thermo-mechanically processed Ti-Al-Mo-V-Cr-Fe alloys, Mater. Sci. Eng. A 576 (2013) 167–177.

[21] M. Ahmed, D.G. Savvakin, O.M. Ivasishin, E.V. Pereloma, The effect of thermo-mechanical processing and ageing time on microstructure and mechanical properties of powder metallurgy near β titanium alloys, J. Alloys Compd. 714 (2017) 610–618.

[22] W. Zhu, J. Lei, C. Tan, Q. Sun, W. Chen, L. Xiao, J. Sun, A novel high-strength β-Ti alloy with hierarchical distribution of α-phase: the superior combination of strength and ductility, Mater. Des. 168 (2019) 107640.

[23] S.A. Mantri, D. Choudhuri, T. Alam, G.B. Viswanathan, J.M. Sosa, H.L. Fraser, R. Banerjee, Tuning the scale of α precipitates in β-titanium alloys for achieving high strength, Scripta Mater. 154 (2018) 139–144.

[24] C.L. Li, P.L. Narayana, N.S. Reddy, S.W. Choi, J.T. Yeom, J.K. Hong, C.H. Park, Modeling hot deformation behavior of low-cost Ti-2Al-9.2Mo-2Fe beta titanium alloy using a deep neural network, J. Mater. Sci. Technol. 35 (2019) 907–916.

[25] R. Liu, B. Wang, J. Li, W. Ma, S. Hu, Deformation behavior and microstructure evolution of powder metallurgy Ti6Al4V alloy during hot compression, J. Mater. Eng. Perform. 28 (2019) 4454–4466.

[26] A. Saboori, A. Abdi, S.A. Fatemi, G. Marchese, S. Biamino, H. Mirzadeh, Hot deformation behavior and flow stress modeling of Ti-6Al-4V alloy produced via electron beam melting additive manufacturing technology in single β-phase field, Mater. Sci. Eng. A 792 (2020) 139822.

[27] F. Yang, B. Gabbitas, Feasibility of producing Ti-6Al-4V alloy for engineering application by powder compact extrusion of blended elemental powder mixtures, J. Alloys Compd. 695 (2017) 1455–1461.

[28] Q. Zhao, F. Yang, R. Torrens, L. Bolzoni, Comparison of hot deformation behaviour and microstructural evolution for Ti-5Al-5V-5Mo-3Cr alloys prepared by powder metallurgy and ingot metallurgy approaches, Mater. Des. 169 (2019) 107682.

[29] Q. Zhao, F. Yang, R. Torrens, L. Bolzoni, In-situ observation of the tensile deformation and fracture behaviour of powder-consolidated and as-cast metastable beta titanium alloys, Mater. Sci. Eng. A 750 (2019) 45–59.

[30] H. Schwab, F. Palm, U. Kuhn, J. Eckert, Microstructure and mechanical properties of the near-beta titanium alloy Ti-5553 processed by selective laser melting, Mater. Des. 105 (2016) 75–80.

[31] H.D. Carlton, K.D. Klein, J.W. Elmer, Evolution of microstructure and mechanical properties of selective laser melted Ti-5Al-5V-5Mo-3Cr after heat treatments, Sci. Technol. Weld. Joi. 24 (2019) 465–473.

[32] W. Chen, C. Chen, X. Zi, X. Cheng, X. Zhang, Y.C. Lin, K. Zhou, Controlling the microstructure and mechanical properties of a metastable β titanium alloy by selective laser melting, Mater. Sci. Eng. A 726 (2018) 240–250.

[33] M. Ahmed, T. Li, G. Casillas, J.M. Cairney, D. Wexler, E.V. Pereloma, The evolution of microstructure and mechanical properties of Ti-5Al-5Mo-5V-2Cr-1Fe during ageing, J. Alloys Compd. 629 (2015) 260–273.

[34] J. Fan, J. Li, H. Kou, K. Hua, B. Tang, Y. Zhang, Influence of solution treatment on microstructure and mechanical properties of a near β titanium alloy Ti-7333, Mater. Des. 83 (2015) 499–507.

[35] J. Fan, J. Li, H. Kou, K. Hua, B. Tang, Y. Zhang, Microstructure and mechanical property correlation and property optimization of a near β titanium alloy Ti-7333, J. Alloys Compd. 682 (2016) 517–524.

[36] J.K. Fan, H.C. Kou, M.J. Lai, B. Tang, H. Chang, J.S. Li, Characterization of hot deformation behavior of a new near beta titanium alloy: Ti-7333, Mater. Des. 49 (2013) 945–952.
[37] R. Dong, J. Li, J. Fan, H. Kou, B. Tang, Precipitation of α phase and its morphological evolution during continuous heating in a near β titanium alloy Ti-7333, Mater. Charact. 132 (2017) 199–204.
[38] G. Yang, H. Kou, J. Yang, J. Li, H. Fu, In-situ investigation on the β to α phase transformation in Ti-45Al-8.5Nb-(W,B,Y) alloy, J. Alloys Compd. 663 (2016) 594–600.
[39] N. Kherrouba, M. Bouabdallah, R. Badji, D. Carron, M. Amir, Beta to alpha transformation kinetics and microstructure of Ti-6Al-4V alloy during continuous cooling, Mater. Chem. Phys. 181 (2016) 462–469.
[40] X. Gao, W. Zeng, S. Zhang, Q. Wang, A study of epitaxial growth behaviors of equiaxed alpha phase at different cooling rates in near alpha titanium alloy, Acta Mater. 122 (2017) 298–309.
[41] J.W. Lu, Y.Q. Zhao, P. Ge, H.Z. Niu, Microstructure and beta grain growth behavior of Ti-Mo alloys solution treated, Mater. Charact. 84 (2013) 105–111.
[42] T. Wang, H.Z. Guo, L.J. Tan, Z.K. Yao, Y. Zhao, P.H. Liu, Beta grain growth behaviour of TG6 and Ti17 titanium alloys, Mater. Sci. Eng. A 528 (2011) 6375–6380.
[43] S.L. Semiatin, P.N. Fagin, M.G. Glavicic, I.M. Sukonnik, O.M. Ivasishin, Influence on texture on beta grain growth during continuous annealing of Ti-6Al-4V, Mater. Sci. Eng. A 299 (2001) 225–234.
[44] P.F. Gao, G. Qin, X.X. Wang, Y.X. Li, M. Zhan, G.J. Li, J.S. Li, Dependence of mechanical properties on the microstructural parameters of TA15 titanium alloy with tri-modal microstructure, Mater. Sci. Eng. A 739 (2019) 203–213.
[45] Z.N. Lei, P.F. Gao, H.W. Li, Y. Cai, Y.X. Li, M. Zhan, Comparative analyses of the tensile and damage tolerance properties of tri-modal microstructure to widmanstatten and bimodal microstructures of TA15 titanium alloy, J. Alloys Compd. 788 (2019) 831–841.
[46] Z.N. Lei, P.F. Gao, H.W. Li, Y. Cai, M. Zhan, On the fracture behavior and toughness of TA15 titanium alloy with tri-modal microstructure, Mater. Sci. Eng. A 753 (2019) 238–246.
[47] P.F. Gao, Y. Cai, M. Zhan, X.G. Fan, Z.N. Lei, Crystallographic orientation evolution during the development of tri-modal microstructure in the hot working of TA15 titanium alloy, J. Alloys Compd. 741 (2018) 734–745.
[48] Y.G. Zhou, W.D. Zeng, H.Q. Yu, An investigation of a new near-beta forging process for titanium alloys and its application in aviation components, Mater. Sci. Eng. A 393 (2005) 204–212.
[49] G.H. Zhang, H.B. Dong, S.L. Zhu, C. Liu, X.P. Yu, Tri-modal structure of TC4-DT alloy through triple heat treatment, Rare Metal Mat. Eng. 45 (2016) 2454–2457.
[50] J.W. Xu, W.D. Zeng, X.Y. Zhang, D.D. Zhou, Analysis of globularization modeling and mechanisms of alpha/beta titanium alloy, J. Alloys Compd. 788 (2019) 110–117.
[51] J.W. Xu, W.D. Zeng, H.Y. Ma, D.D. Zhou, Static globularization mechanism of Ti-17 alloy during heat treatment, J. Alloys Compd. 736 (2018) 99–107.
[52] J.W. Xu, W.D. Zeng, Z.Q. Jia, X. Sun, J.H. Zhou, Static globularization kinetics for Ti-17 alloy with initial lamellar microstructure, J. Alloys Compd. 603 (2014) 239–247.
[53] D. Banerjee, J.C. Williams, Perspectives on titanium science and technology, Acta Mater. 61 (2013) 844–879.
[54] F. Geng, M. Niinomi, M. Nakai, Observation of yielding and strain hardening in a titanium alloy having high oxygen content, Mater. Sci. Eng. A 528 (2011) 5435–5445.
[55] Q. Yu, L. Qi, T. Tsuru, R. Traylor, D. Rugg, J.W. Morris Jr., M. Asta, D.C. Chrzan, A.M. Minor, Metallurgy. Origin of dramatic oxygen solute strengthening effect in titanium, Science 347 (2015) 635–639.
[56] S.W. Wu, G. Wang, Q. Wang, Y.D. Jia, J. Yi, Q.J. Zhai, J.B. Liu, B.A. Sun, H.J. Chu, J. Shen, P.K. Liaw, C.T. Liu, T.Y. Zhang, Enhancement of strength-ductility trade-off in a high-entropy alloy through a heterogeneous structure, Acta Mater. 165 (2019) 444–458.
[57] R.X. Zheng, M.W. Liu, Z. Zhang, K. Ameyama, C.L. Ma, Towards strength-ductility synergy through hierarchical microstructure design in an austenitic stainless steel, Scripta Mater. 169 (2019) 76–81.
[58] C. Zhang, C.Y. Zhu, K. Vecchio, Non-equiatomic FeNiCoAl-based high entropy alloys with multiscale heterogeneous lamella structure for strength and ductility, Mater. Sci. Eng. A 743 (2019) 361–371.
[59] X.L. Wu, Y.T. Zhu, Heterogeneous materials: a new class of materials with unprecedented mechanical properties, Mater. Res. Lett. 5 (2017) 527–532.
[60] W. Chrominski, M. Lewandowska, Precipitation phenomena in ultrafine grained Al-Mg-Si alloy with heterogeneous microstructure, Acta Mater. 103 (2016) 547–557.
[61] X. Wu, M. Yang, F. Yuan, G. Wu, Y. Wei, X. Huang, Y. Zhu, Heterogeneous lamella structure unites ultrafine-grain strength with coarse-grain ductility, Proc. Natl. Acad. Sci. 112 (2015) 14501–14505.
[62] W. Guo, Z.R. Pei, X.H. Sang, J.D. Poplawsky, S. Bruschi, J. Qu, D. Raabe, H.B. Bei, Shape-preserving machining produces gradient nanolaminate medium entropy alloys with high strain hardening capability, Acta Mater. 170 (2019) 176–186.
[63] J. Gao, J. Nutter, X. Liu, D. Guan, Y. Huang, D. Dye, W.M. Rainforth, Segregation mediated heterogeneous structure in a metastable beta titanium alloy with a superior combination of strength and ductility, Sci. Rep. 8 (2018) 7512.
[64] S. Shin, C. Zhu, C. Zhang, K.S. Vecchio, Extraordinary strength-ductility synergy in a heterogeneous-structured β -Ti alloy through microstructural optimization, Mater. Res. Lett. 7 (2019) 467–473.
[65] R.X. Zheng, G.D. Li, Z. Zhang, Y.T. Zhang, S.Y. Yue, X. Chen, K. Ameyama, C.L. Ma, Manipulating the powder size to achieve enhanced strength and ductility in harmonic structured Al alloy, Mater. Res. Lett. 7 (2019) 217–224.
[66] G. Chen, J.W. Qiao, Z.M. Jiao, D. Zhao, T.W. Zhang, S.G. Ma, Z.H. Wang, Strength-ductility synergy of $Al_{0.1}$CoCrFeNi high-entropy alloys with gradient hierarchical structures, Scripta Mater. 167 (2019) 95–100.
[67] C. Tan, Q. Sun, L. Xiao, Y. Zhao, J. Sun, Characterization of deformation in primary α phase and crack initiation and propagation of TC21 alloy using in-situ SEM experiments, Mater. Sci. Eng. A 725 (2018) 33–42.
[68] W. Zhu, J. Lei, Z. Zhang, Q. Sun, W. Chen, L. Xiao, J. Sun, Microstructural dependence of strength and ductility in a novel high strength β titanium alloy with bi-modal structure, Mater. Sci. Eng. A 762 (2019) 138086.
[69] Z. Sun, X. Mao, H. Wu, H. Yang, J. Li, Tri-modal microstructure and performance of TA15 Ti-alloy under near-β forging and given subsequent solution and aging treatment, Mater. Sci. Eng. A 654 (2016) 113–123.